

Columbia University

IN THE CITY OF NEW YORK

5-235 RESONANCE CROSS SECTIONS AND  
GASEOUS CORE REACTOR CALCULATIONS

N 66-16282

FACILITY FORM 502

(ACCESSION NUMBER)

(THRU)

(PAGES)

(CODE)

(NACA OR ON-TAX OR AD NUMBER)

(CATEGORY)

Günter K. Tamm

GPO PRICE \$

CFSTI PRICE(S) \$

Hard copy (HC) 4.00

Microfiche (MF) 75

ff 853 July 65



PLASMA LABORATORY  
SCHOOL OF ENGINEERING AND APPLIED SCIENCE  
NEW YORK 27, N.Y.

U-235 RESONANCE CROSS SECTIONS AND  
GASEOUS CORE REACTOR CALCULATIONS

Günter W. Tumm\*

August 1965

PLASMA RESEARCH LABORATORY

REPORT NO. 22

Columbia University  
New York, New York

\*NASA International Fellow in Space Science;  
Columbia University.

This study was supported in part by the Air  
Force Office of Scientific Research under  
Contracts AF-49(638)1254 and AF-49(638)1634.

## TABLE OF CONTENTS

	<u>Page</u>
1. INTRODUCTION	1
2. THEORY	3
2.1 Calculational Methods (the HRG-Program)	3
2.2 Functional Dependence of Resonance Integrals on Temperature and Dilution	12
3. INTERMEDIATE RESULTS	17
3.1 Resonance Integrals of U-238 and Comparison with Experiment	17
3.2 Resonance Integrals of U-235 by HRG-Program	20
3.3 Revision of HRG-Program	20
3.4 Resonance Integrals of U-235 by Revised HRG-Program and Comparison with Experimental Results	22
4. U-235 RESONANCE CROSS SECTION CALCULATIONS	25
4.1 Selection of Gaseous Core Reference System	25
4.2 Final Cross Section Calculations and Comparison with LASL 6-and-16 Group Cross Sections	26
4.3 Effect of Buckling and Dilution Slowing Down Flux	29
4.4 Estimate of Doppler Coefficient of Reactivity	33
5. APPLICATION TO SPECIFIC GASEOUS CORE REACTOR SYSTEMS	36
5.1 Check of Homogenization Assumption and Comparison with Previous Theoretical Results	40
5.1.1 Comparison with previously calculated critical masses	40
5.1.2 Homogenization assumption (spatial dependence)	44

5.1.3	Energy dependence of slowing down flux	47
5.2	Doppler Temperature Coefficient of Reactivity	49
5.3	Comparison with Measured Critical Masses	52
5.3.1	For spherical systems	52
5.3.2	For Cylindrical systems	54
5.4	Variation of Critical Mass Under "Interior" and "Exterior" Fuel Compression	59
5.4.1	Fuel compression without hydrogen	60
5.4.2	Fuel compression with hydrogen	68
6.	CONCLUSION	78
	REFERENCES	98
	ACKNOWLEDGEMENTS	100

## LIST OF FIGURES

		<u>Page</u>
Fig. 1	Effective Resonance Integrals of U-238 $T=300^{\circ}\text{K}$ ; Energy Range: $6.5\text{ev} \div 2.61\text{ Kev}$	18
Fig. 2	Effective Resonance Integrals of U-235 for Absorption and Fission $T=300^{\circ}\text{K}$ ; Energy Range: $1.125\text{ev} \div 3.36\text{ Kev}$	18
Fig. 3	Slowing Down Flux for Various Dilutions	31
Fig. 4	Slowing Down Flux for Various Bucklings	32
Fig. 5	$m_{\text{cr}} = f(\text{cavity radius})$	38
Fig. 6	$m_{\text{cr}} = f(\text{mesh width in cavity})$	39
Fig. 7	$m_{\text{cr}} = f(nh/\nu \text{ in cavity})$	42
Fig. 8	Radial Dependence of Thermal Flux	45
Fig. 9	Comparison of Slowing Down Fluxes	48
Fig. 10	Configuration of Cylindrical Experimental Reactors	56
Fig. 11	Basic Compression Cases	61
Fig. 12	Interior and Exterior Fuel Compression Without Hydrogen	64
Fig. 13	Thermal Fluxes for Compression Cases (Without Hydrogen)	66
Fig. 14	Interior Fuel Compression with Hydrogen	70
Fig. 15A	Fast and Thermal Flux for $p_{\text{int}} = 1/2$	71
Fig. 15B	Fast and Thermal Flux for $p_{\text{int}} = 5/8$	72

Fig. 15C	Fast and Thermal Flux for $p_{int} = 9/10$	73
Fig. 16	Exterior Fuel Compression with Hydrogen	76
Fig. 17	Thermal Fluxes for Exterior Compression	77

## LIST OF TABLES

		<u>Page</u>
Table 1	Doppler widths at various temperatures and resonance energies	79
Table 2	Some Resonance Data	80
Table 3	Effective Resonance Integrals for U-238	81
Table 4A	U-235 Effective Resonance Integrals for Resolved Region	82
Table 4B	U-235 Effective Resonance Integrals for Resolved and Unresolved Region	83
Table 5	Absorption and Fission Cross Sections in the U-235 Unresolved Region	84
Table 6A	Corrected Effective Resonance Integrals for U-235 (unresolved region)	85
Table 6B	Corrected Effective Resonance Integrals for U-235 (resolved and unresolved region)	86
Table 7	U-235 Resonance Cross Sections at Various Temperatures	87
Table 8A	Comparison of LASL-6 group with HRG-6 group Cross Sections	90
Table 8B	Comparison of LASL-16 group with HRG- Resonance Cross Sections	91
Table 9	Influence of Buckling and Dilution on the HRG-Resonance Cross Sections	92
Table 10	Radial Dependence of Resonance Fluxes (Case A6)	93

Table 10A	Radial Dependence of Thermal Fluxes (Case C5)	94
Table 11	Data for Spherical Experimental Reactors	95
Table 12	Data for Cylindrical Experimental Reactors	97



## 1. INTRODUCTION

The problem of determining the effective resonance integrals and the resonance cross sections of U-235 at elevated temperatures ( $> 2000^{\circ}\text{K}$ ) arises in calculations concerning advanced reactor concepts using gaseous fissionable materials. An assumption frequently made in the calculation of gaseous core reactors is to neglect the broadening of the resonances, thus neglecting entirely the Doppler coefficient of reactivity.<sup>1,2</sup> Although it can be expected that the temperature coefficients are small, they cannot be neglected in more sophisticated kinetic calculations.

For the calculations, using the HRG-program, a revised version of the GAMI-program,<sup>3</sup> and the CRAM-program,<sup>11</sup> a gaseous core reference system was selected and a complete new set of resonance cross sections was determined using the Adler-Nordheim method. Variations in buckling and slowing down flux were investigated.

In order to establish the validity of the results certain checks and double checks were performed, e.g. comparison of the measured and calculated infinite dilution integrals of U-238 and U-235, and comparison of calculated and LASL-16 group resonance cross section.<sup>10</sup>

Furthermore, measured critical masses from experiments which can be assumed to be representative for gaseous core reactors were re-evaluated using the new set of resonance cross sections.

---

<sup>10</sup> For numbered references, see p. 98.

Finally an extensive investigation has been made into applying the new resonance data to specific gaseous core reactor systems. Critical masses were compared with previous theoretical results and some phenomena with respect to fuel compression and the presence of hydrogen within the reactor cavity were discussed.

## 2. THEORY

### 2.1 Calculational Methods

The theory presented in this section (using the notation of Ref. 4) is the one applied in the HRG-program which determines multi-group cross sections within the energy range 10 MeV to 0.414 eV using the  $B_1$ -slowing down approximation.

The major part of this report concerns the Doppler broadening of resonances, thus the behavior of the effective resonance integrals under temperature changes. Since all conclusions concerning the resonance cross sections are drawn from this behavior, only the theory in connection with the effective resonance integrals shall be given.

#### a. The effective resonance integral (resolved region)

The effective resonance integral for absorption or fission is defined as the absorption-or fission cross section, integrated over lethargy and assuming the flux has its asymptotic value, which produces the same amount of absorptions or fissions as actually takes place in the resonance.

Two cases are generally considered: The narrow resonance approximation (NR) where the lethargy width of the resonance is small compared to the lethargy increment per collision for all nuclei present, and the infinite mass narrow resonance approximation (IM) in which the slowing down due to the absorber is entirely neglected.

In the following only the NR case is considered; the treatment of the IM case is similar. The interference effect between resonances will be considered in Part c of this section.

The absorption and fission cross section in the resonance region is customarily split into two parts: a slowly varying cross section and a resonance cross section. The latter is determined by the effective resonance integrals:

$$\sigma^{\text{resonance}} = \frac{1}{\Delta n} \sum_{i \text{ in } n} I_i \quad (1)$$

$I_i$  = effective resonance integral

$\Delta n$  = lethargy width of the group for which the resonance cross section is to be determined.

The resonance integral itself is divided into a volume and a surface term. For a homogeneous mixture of scatterer and resonance absorber the surface term is zero by definition. Throughout this paper it will be assumed that the surface term is negligibly small. In order to understand the approximation involved some features of gaseous core reactors have to be sketched out briefly. Gaseous core reactors which are generally considered only in connection with advanced propulsion devices consist of a (cylindrical) cavity filled with gaseous uranium and gaseous hydrogen surrounded by a reflector. In general, the cavity materials uranium and hydrogen are separated, either hydrogen surrounds an inner gaseous uranium core ("coaxial flow device") or gaseous uranium surrounds an inner hydrogen core ("vortex flow device"). Thus it is theoretically possible to define a "surface" of the uranium region. However, one of the main properties of

gaseous core reactors is that the neutron mean free path within the two gaseous substances uranium and hydrogen is large compared with the cavity dimensions. This is true except for the extreme cases in the "coaxial flow device" where the inner uranium region has a radius very small compared to the cavity radius. Therefore, for almost all cases occurring in actual gaseous core reactor designs, the surface term of the effective resonance integral which takes into account the flux depression within the uranium "lump" can be neglected.

However, the homogeneity assumption not only concerns the cavity but the total reactor, i.e., it is assumed that uranium, reflector, and hydrogen atoms form a homogeneous mixture. This assumption is investigated in Secs. 5.1.2 and 5.1.3 and proved to be valid at least with respect to the here interesting resonance fluxes.

The resonance integral for the resolved resonances for the non-broadened case is given by:

$$I_{c \text{ res}} = \int \frac{\sigma_p \left[ \sigma_o \frac{\Gamma}{\Gamma} (1 + x^2)^{-1} \right]}{\sigma_o (1 + x^2)^{-1} + (\sigma_o \sigma_p i)^{\frac{1}{2}} 2x(1 + x^2)^{-1} + \sigma_p} du \quad (2)$$

(for capture)

The interference term contains a quantity  $i$ :

$$i = g_J \frac{\Gamma_n}{\Gamma} \frac{\sigma_{p_a}}{\sigma_p}$$

$$\frac{\sigma_{p_a}}{\sigma_p} = \frac{N_a \sigma_{p_a}}{N_a \sigma_{p_a} + N_m \sigma_s}$$

$$= \frac{1}{1 + \frac{\sigma_s}{\sigma_{p_a}} \cdot \frac{N_m}{N_a}} \quad (3)$$

Thus interference can be neglected if  $\Gamma_n \ll \Gamma$ , i.e., for a purely absorbing resonance, or a very dilute mixture with  $N_m \gg N_a$ . These two conditions are not applicable in the case considered here. Fortunately there exists a third condition under which the interference term can be neglected, i.e., for extreme Doppler broadening. To explain this, the Doppler broadened line shape has to be introduced:

$$\psi(\xi, x) = (4\pi)^{-\frac{1}{2}} \xi \int_{-\infty}^{\infty} \frac{\exp[-\frac{1}{4}\xi^2(x-y)^2]}{1+y^2} dy \quad (4)$$

where

$$x = \frac{E - E_i}{\Gamma/2} ; \quad y = \frac{E' - E_i}{\Gamma/2}$$

$$\Delta = \left( \frac{4mTE_i}{M} \right)^{\frac{1}{2}} \quad (5)$$

$$\xi = \frac{\Gamma}{\Delta} \quad \Delta = \text{Doppler width of resonance} \quad (6)$$

$\Gamma = \text{total width of resonance}$

$$\beta = \sigma_p / \sigma_o$$

$\sigma_o$  = total cross section at  $x = 0$

$\sigma_p$  = nonresonant scattering cross section per absorber atom.

Equation (4) is obtained with an assumption which has to be mentioned in connection with the considered high temperatures.

Let  $v$  be the neutron velocity, and

$v_r$  the relative velocity between neutron and target.

The assumption is that  $v + v_r$  is approximated by  $2v$ . This introduces a problem for low lying resonances and very high temperatures.

$$E_r = \frac{1}{2}m'(v - V)^2 \quad : \quad E_r = \text{energy corresponding to } v_r$$

$m'$  = neutron reduced mass

$V$  = target velocity

$$\text{but} \quad V = \sqrt{\frac{2E_t}{M}} \quad \text{and} \quad v = \sqrt{\frac{2E}{m}}$$

$$\text{then} \quad \frac{V}{v} = \sqrt{\frac{2 \frac{3}{2} k T m}{M 2 E}} \approx \left( \frac{k T}{M E} \right)^{\frac{1}{2}}$$

For  $T = 3.5 \text{ eV} (\approx 40,000^\circ \text{K})$  and  $E = 5 \text{ eV}$ ,  $V \approx 0.02 v$ .

Therefore in the above-mentioned approximation an error of  $\approx 1\%$  is introduced. These errors are only significant for low lying resonances where the Doppler effect is small. It can be concluded that the effect of high target velocities is quite small.

Going back to the interference effect, Dresner<sup>4</sup> has shown that for  $\xi \ll 1$  and  $\beta \gg \xi^2/\epsilon$  the interference term can be neglected.

For the 19.3 eV - U-235 resonance at  $T = 10,000^\circ\text{K}$ ,

$$\Gamma = 0.099 \text{ eV} ; \Delta = 0.54 \text{ (from Table 1)}$$

$$\xi = \frac{0.099}{0.54} = 0.183 \quad \text{which is} < 1.0 .$$

$$\sigma_p = 10^4 ; \sigma_o = 200. \rightarrow \beta = 50 \rightarrow \beta > \frac{\xi^2}{6} = 0.006$$

The above conditions are fulfilled for all U-235 resonances and for high temperatures.

In general the Doppler broadened counterpart of the interference scattering line shape can be neglected if  $\xi < 1$  and  $x^2 \ll 6/\xi^2$ . In the center of the line this is always true and in the present case for  $6/\xi^2$  very large this is also true far out into the resonance wings. Therefore, because the wings contribute very little to the total resonance integral, the interference effect can be neglected.

The HRG-program uses the numerical method proposed by Adler et al<sup>5</sup> to compute the resonance integral. The effective capture resonance integral in the resolved region is given by:

$$I_c = \frac{\sigma_p \Gamma_\gamma}{E_i} \int_0^\infty \frac{\psi(\xi, x) dx}{\psi(\xi, x) + \beta} \equiv \frac{\sigma_p \Gamma_\gamma}{E_i} J(\xi, \beta) \quad (\text{NR}) \quad (7)$$

For the effective absorption resonance integral  $\Gamma_\gamma$  is replaced by  $(\Gamma_\gamma + \Gamma_f)$ . In the IM-approximation the following substitutions are made:



$$\sigma_p \rightarrow \sigma_s^*$$

$\sigma_s^*$  = moderator cross section  
per absorber atom

$$\beta = \frac{\sigma_s^*}{\sigma_o} \cdot \Gamma/\Gamma_\gamma$$

The function  $J(\xi, \beta)$  is tabulated and the program interpolates between the tabulated values.\*

b. The effective resonance integral (unresolved region)

Later in the report it will be shown that the correct determination of the unresolved part of the effective resonance integral is unnecessary. Only the infinite dilution integral at room temperature needs to be determined.

The infinite dilution integral for one resonance is given by:

$$I_{c\infty} = \frac{\pi}{2} \sigma_o \frac{\Gamma_\gamma}{E_i} \quad (\text{for capture}) \quad (8)$$

Then the contribution to the total resonance integral  $I_{unres}$  for a range  $\Delta E$  around  $E_i$  is given by:

$$\Delta I_{cunres\infty} = \frac{\pi}{2E_i} \overline{\sigma_o \Gamma_\gamma} \cdot \frac{\Delta E}{D}$$

$$\overline{\sigma_o \Gamma_\gamma} = \text{averaged over statistical distribution}$$

$D$  = average level spacing (assumed to be constant)

\* Although the  $\xi$ -spacings for very small  $\xi$ , i.e., for very high temperatures, are wide, the program determines the interpolated values rather accurate at least for the range of the resolved resonances. As shown later the interpolation is not used for the inaccurate range of the unresolved resonances.

Then  $I_{\text{unres}}$  is obtained by integrating over all energies from some cut-off energy  $E_c$  to infinity.

$$I_{\text{cunres}}^{\infty} = \frac{\pi}{2D} \int_{E_c}^{\infty} \overline{\sigma_o \Gamma_{\gamma}} \frac{dE}{E} \quad (9)$$

The same procedure can be taken for the case of finite dilution. Here the NR approximation is exclusively used. Starting with

$$I_{\text{cunres}} = \frac{\sigma_p \Gamma_{\gamma}}{E_i} J(\xi, \beta) \quad (\text{for one resonance})$$

one obtains, and now taking into account the statistical distribution of neutron widths  $p(y)dy$ ,

$$I_{\text{cunres}} = \frac{\sigma_p \Gamma_{\gamma}}{D} \int_{E_c}^{\infty} \frac{dE}{E} \int_0^{\infty} p(y) dy J(\xi, \beta) \quad (10)$$

with 
$$p(y)dy = \frac{1}{\sqrt{2\pi y}} \exp(-y/2) dy \quad (11)$$

$$\text{with } y = \Gamma_n^o / \langle \Gamma_n^o \rangle$$

$$\Gamma_n^o = \Gamma_{nE_i}^{-\frac{1}{2}} \quad \text{the reduced neutron width and}$$

$$\langle \Gamma_n^o \rangle \quad \text{the average reduced neutron width.}$$

Some resonance data for U-235 and U-238 taken from the GAMI-library are presented in Table 2. It can be seen that for U-235, the nuclide of main interest, all resonances in the resolved region, with the exception of the 10.6 eV-

resonance, are calculated according to the IM-approximation. Although it was intended to use this approximation only for conventional reactor systems there is no doubt that the temperature range can be extended up to temperatures in the order of eV, because their extreme Doppler broadening occurs and this makes the IM-approximation even more applicable. Because the problem of determining the resonance integral in the unresolved region will be solved by a different method there is no need to be concerned about the NR-approximation, inherent in the unresolved resonance calculation, at extreme temperatures.

An example for the accuracy of the IM-approximation for the 36.9 eV-resonance in U-238 is given below:  
for 1:1 atomic ratio H/U-238 (at room temperature):  
(with  $p$  = resonance escape probability):

resonance	$1-p$ (exact)	$1-p_0$ (variational*)	$1-p$ (NR)	$1-p$ (IM)
36.9 eV	0.05820	0.05682	0.04739	0.06110

### c. Resonance interaction effect

If resonances are closely spaced such that the flux does not recover its asymptotic spectrum between the resonances the flux perturbations induced by the higher (in energy) lying resonance affect the resonance escape probability at the lower lying resonance. R. Schermer and N. Corngold<sup>6</sup> show that a scattering resonance causes a positive interference effect, whereas an absorption resonance leads to a negative interference effect. Positive and negative interference is defined by the

---

\* Calculated by a variational approach by N. Corngold, Proc. of the Phys. Soc., A, Vol. LXX, p. 793, 1957.

parameter  $\rho_2$ :

$$\rho_2 = \frac{\text{captures due to interference}}{\text{non-interference captures}} = \frac{\text{total captures}}{\text{non-interference captures}} - 1$$

Therefore an energetically higher lying scattering resonance gives rise to a higher amount of captures in the lower lying capture resonance compared to calculations where interference is neglected. The opposite result is obtained if the higher lying resonance is of absorption type.

The calculations show that the interaction effect depends on the level spacing ( $\ell$ ), the energy decrement per collision in moderator ( $\xi_m$ ) and resonance absorber ( $\xi_u$ ). For  $\ell \rightarrow 0$  the interaction effect decreases for resonance width  $> \xi_u$  (e.g., U-235). Furthermore, the effect increases for heavier moderators because of the smaller  $\xi_m$ 's for higher masses and decreases for mixtures with larger moderator: absorber - atomic ratios.

However, because of the close results between measured and calculated resonance integrals, neglecting interference,\* it can be assumed that the interference effects of opposite sign cancel, and by neglecting this effect only a small error is introduced.

## 2.2 Functional Dependence of Resonance Integrals On Temperature and Dilution

In this section only the effective capture resonance integral in the NR-approximation is considered. All equations are also applicable on the absorption resonance integral.

---

\* Later in this report this is verified for U-238 and the fission integral of U-235.

It is easy to verify that Eq. 7 reduces to the infinite dilution resonance integral for  $\sigma_p \rightarrow \infty$ .

$$I_c = \frac{\sigma_p \Gamma \gamma}{E_i} \int_0^\infty \frac{\psi(\xi, x) dx}{\psi(\xi, x) + \beta} \quad (7)$$

$$= \frac{1}{2} \frac{\Gamma \gamma}{E_i} \int_{-\infty}^\infty \frac{\psi}{\psi/\sigma_p + 1/\sigma_0} dx \quad (7a)$$

then:

$$\begin{aligned} \lim_{\sigma_p \rightarrow \infty} I_{c^\infty} &= \frac{1}{2} \frac{\Gamma \gamma}{E_i} \left\{ \lim_{\sigma_p \rightarrow \infty} \int_{-\infty}^\infty \frac{\psi}{\psi/\sigma_p + 1/\sigma_0} dx \right\} \\ &= \frac{1}{2} \frac{\Gamma \gamma}{E_i} \sigma_0 \int_{-\infty}^\infty \psi(\xi, x) dx = \frac{\pi}{2} \sigma_0 \frac{\Gamma \gamma}{E_i} \\ I_{c^\infty} &= \frac{\pi}{2} \sigma_0 \frac{\Gamma \gamma}{E_i} \quad (\text{the infinite dilution resonance integral}). \end{aligned} \quad (12)$$

An obvious conclusion, drawn from Eq. 7a, is that the effective resonance integral increases with increasing  $\sigma_p$ , i.e., with increasing scattering cross section per absorber atom or increasing dilution. It reaches its asymptotic value in the infinite dilution integral.

The same is true for the resonance integral in the unresolved region (Eq. 10) because

$$\int_{E_c}^\infty \frac{dE}{E} \int_0^\infty p(y) dy \quad \text{does not depend on the dilution.}$$

The temperature dependence of the effective resonance integral, i.e., its dependence on the variable  $\xi$ , can be evaluated in the following way. For the resolved region one obtains:

$$\frac{\partial I_{\text{res}}}{\partial \xi} = \sigma_P \frac{\Gamma \gamma}{E_i} \int_0^\infty \left[ \frac{\partial}{\partial \xi} \left( \frac{\psi(\xi, x)}{\psi(\xi, x) + \beta} \right) \right] dx \quad (13)$$

$$= \sigma_P \frac{\Gamma \gamma}{E_i} \int_0^\infty \left[ \frac{(\psi + \beta) \frac{\partial \psi}{\partial \xi} - \psi \frac{\partial \psi}{\partial \xi}}{(\psi + \beta)^2} \right] dx$$

$$= \sigma_P \frac{\Gamma \gamma}{E_i} \beta \int_0^\infty \frac{\partial \psi / \partial \xi}{(\psi + \beta)^2} dx \quad (13a)$$

$\psi(\xi, x)$  is given by Eq. 4. Then:

$$\frac{\partial \psi}{\partial x} = - \frac{\xi^3}{4\sqrt{\pi}} \int_{-\infty}^\infty (x - y) \frac{\exp[-\frac{1}{4}\xi^2(x - y)^2]}{1 + y^2} dy$$

$$\frac{\partial^2 \psi}{\partial x^2} = - \frac{\xi^3}{4\sqrt{\pi}} \psi(\xi, x) + \frac{\xi^5}{8\sqrt{\pi}} \int_{-\infty}^\infty (x - y)^2 \frac{\exp[-\frac{1}{4}\xi^2(x - y)^2]}{1 + y^2} dy \quad (14)$$

In addition:

$$\frac{\partial \psi}{\partial \xi} = \frac{1}{2\sqrt{\pi}} \psi(\xi, x) - \frac{\xi^2}{4\sqrt{\pi}} \int_{-\infty}^\infty (x - y)^2 \frac{\exp[-\frac{1}{4}\xi^2(x - y)^2]}{1 + y^2} dy \quad (15)$$

By comparing Eqs. 14 and 15 one obtains:

$$\frac{\partial \psi}{\partial \xi} = - \frac{2}{\xi^3} \frac{\partial^2 \psi}{\partial x^2} \quad (16)$$

Introducing this into Eq. 13a it follows:

$$\frac{\partial I_{\text{res}}}{\partial \xi} = - \sigma_p \frac{\Gamma \gamma}{E_i} \beta \frac{2}{\xi^3} \int_0^\infty \frac{\partial^2 \psi / \partial x^2}{(\psi + \beta)^2} dx$$

with

$$A = \sigma_p \frac{\Gamma \gamma}{E_i} \beta$$

and performing the partial integration:

$$\frac{\partial I_{\text{res}}}{\partial \xi} = A \left[ \frac{2}{\xi^3} \frac{\partial \psi / \partial x}{(\psi + \beta)^2} \right]_0^\infty + \frac{2}{\xi^3} \int_0^\infty \frac{2(\partial \psi / \partial x)^2}{(\psi + \beta)^3} dx \quad ]$$

because  $\frac{\partial \psi}{\partial x} = 0$  at  $x = 0$  and  $x = \infty$ ,

it follows:

$$\frac{\partial I_{\text{res}}}{\partial \xi} = - \frac{4A}{\xi^3} \int_0^\infty \left( \frac{\partial \psi}{\partial x} \right)^2 \cdot (\psi + \beta)^{-3} dx. \quad (17)$$

All terms on the r.h.s. are positive, thus

$$\frac{\partial I_{\text{res}}}{\partial \xi} < 0 \quad (18)$$

Because  $\xi$  is inversely proportional to the temperature, it follows that the effective resonance integral increases with increasing temperature. Again, the same dependence can be found in the effective resonance integral in the unresolved region:

$$I_{\text{unres}} = \frac{\sigma_p \Gamma \gamma}{D} \int_{E_c}^{\infty} \frac{dE}{E} \int_0^{\infty} p(y) dy \quad J(\xi, \beta) \quad (10)$$

with

$$J(\xi, \beta) = \int_0^{\infty} \frac{\psi(\xi, x) dx}{\psi(\xi, x) + \beta} .$$

Thus:

$$\frac{\partial I_{\text{unres}}}{\partial \xi} = \frac{\sigma_p \Gamma \gamma}{D} \int_{E_c}^{\infty} \frac{dE}{E} \int_0^{\infty} p(y) dy \int_0^{\infty} \left[ \frac{\partial}{\partial \xi} \left( \frac{\psi(\xi, x)}{\psi(\xi, x) + \beta} \right) \right] dx \quad (19)$$

because  $\int_{E_c}^{\infty} \frac{dE}{E} \int_0^{\infty} p(y) dy$  is greater than zero,

the same result as found in Eq. 17 - with different constants - is obtained, i.e.,

$$\frac{\partial I_{\text{unres}}}{\partial \xi} < 0 . \quad (20)$$

So also the unresolved resonance integral has to increase with increasing temperature.



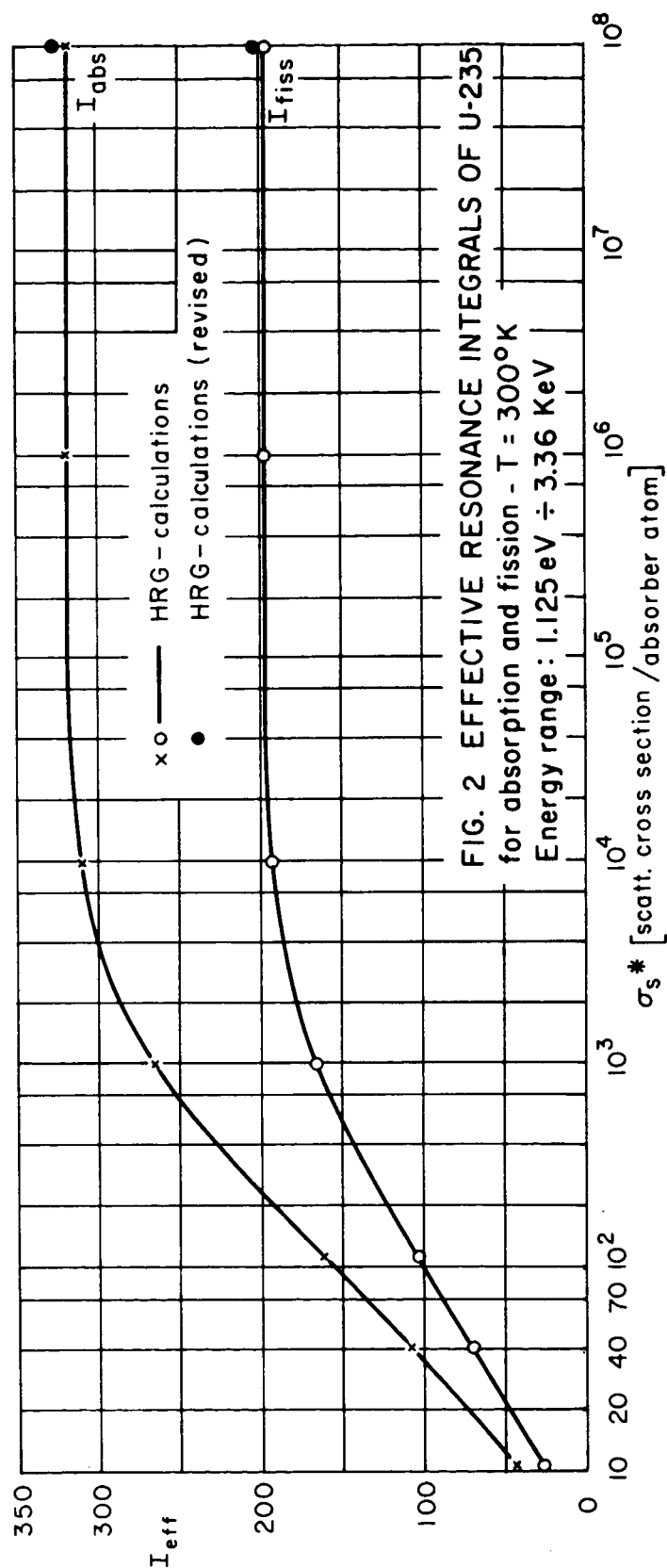
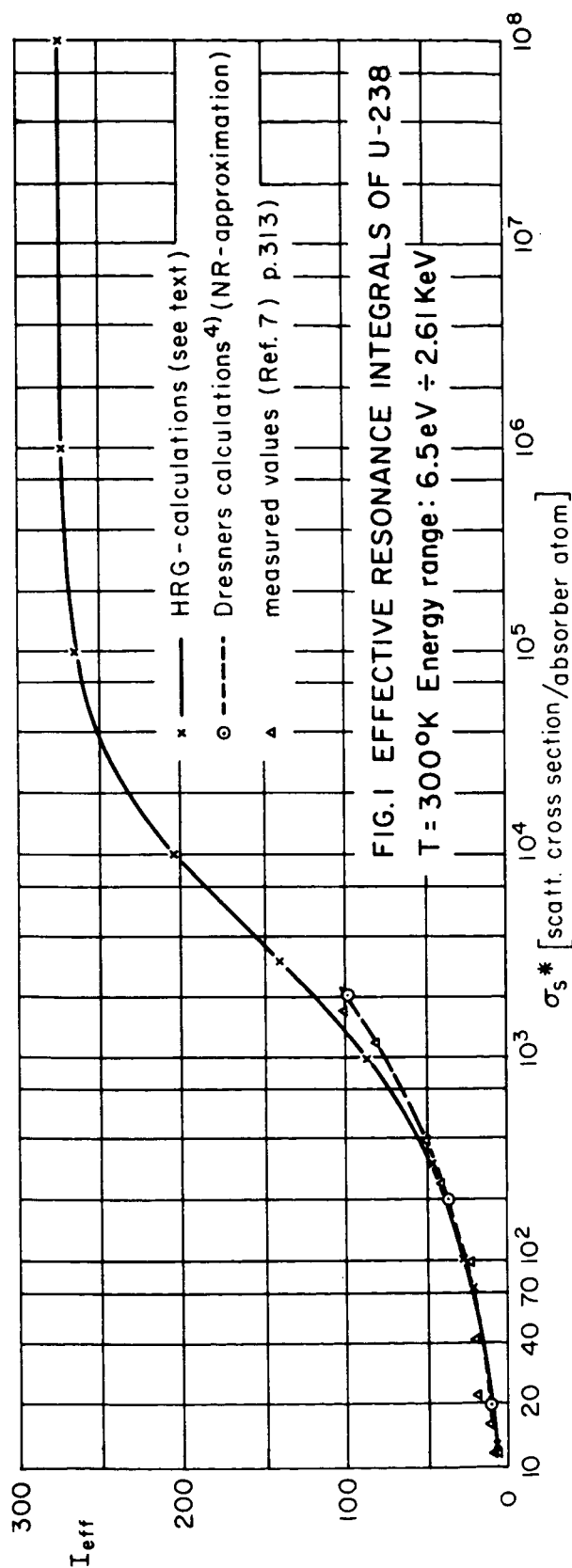
### 3. INTERMEDIATE RESULTS

#### 3.1 U-238 Resonance Integrals and Comparison with Experiment

In order to establish the validity of the final results certain checking calculations were performed, one of which was the calculation of U-238 effective resonance integral. Although some of the results are already available in the literature these calculations were important because they gave the first indication that the unresolved resonance calculation breaks down for extreme temperatures.

The calculations, using the HRG-program (unrevised for higher temperatures), are summarized in Table 3. In Fig. 1 the effective resonance integrals for  $T = 300^\circ\text{K}$  are plotted against  $\sigma_s^*$  together with Dresner's calculations<sup>4</sup> and measured values. Figure 1 shows that the resonance integral first increases exponentially but has an inflection point around  $\sigma_s^* = 5 \times 10^3$  and goes for higher  $\sigma_s^*$  to its asymptotic value. The agreement with experiment and Dresner's results at low  $\sigma_s^*$  is good but diverges from Dresner's results at  $\sigma_s^*$  around  $10^3$ . This is due to the fact that Dresner's resonance calculation was done in the NR-approximation, whereas the HRG-program computes 6 of the lower lying resonances (6.68; 21.0; 36.8; 66.3; 102.8 eV) in the IM-approximation which leads to a higher resonance integral (see Ref. 5, Table 3).

Another check can be done on the value of the infinite dilution integral of U-238. A standard value is  $280 \pm 4$  barns.<sup>4</sup> Because the HRG-program computes resonance integrals of U-238 only between 6.5 eV and 2.61 KeV the fast and thermal absorption cross sections have to be added to the computed value:



energy range	$\overline{\sigma}_a^*$	$\Delta u$	$I_{eff}$
thermal $\div$ 6.5 eV	0.63	5.56	3.5
6.5 eV $\div$ 2.61 KeV	—	—	275.01
2.61 KeV $\div$ 10 MeV	0.46	8.00	3.68

$$\underline{\Sigma: 282.19 \text{ barns}}$$

\* Cross sections averaged  
from HRG-library data

Because the slowly varying cross section adds only a negligible amount to this value the agreement between the measured and the computed value is very good.

The important behavior in the calculated U-238 resonance integrals is the decrease of the unresolved resonance contribution with increasing temperature. This decrease becomes larger for increasing  $\sigma_s^*$ . However, Eq. 20 shows that just the opposite behavior must be expected. This indicates a breakdown of the unresolved resonance calculation at higher temperatures.

The reason for this effect is inherent in the calculational method because in the HRG-program the second integral of Eq. 10 is approximated by Simpson's rule. In order to cure this deficiency the number of pivotal points was increased by a factor of 100. Although the results improved considerably for U-238 (e.g.,  $T = 10.000^\circ\text{K}$ ;  $\sigma_s^* = 10^8 \rightarrow \text{RR} + \text{URR} = 273.98$ ;  $(\text{RR} + \text{URR})_{\text{improved}} = 275.00$ ) this still was not enough for the broad unresolved resonance region of U-235. (e.g.,  $10.000^\circ\text{K}$ ;  $\sigma_s^* = 10^8$ ;  $I_f = 179.26$ ;  $(I_f)_{\text{improved}} = 180.48$ ) Even higher order divisions would not cure (within reasonable limits of computer time) the error due to the numerical integration.

This was the reason for employing a different method for computing the unresolved resonance contribution. No attempt was made to recalculate the resonance integrals of U-238 at higher temperatures.

### 3.2 U-235 Resonance Integrals by HRG-Program

Although, as indicated in the previous section, the calculation of the effective resonance integrals of U-235 in the unresolved region and at higher temperatures is erroneous, they shall be listed in Table 4B in order to show the relative increase of the error with the increasing width of the unresolved region (20 eV to 3 KeV in U-235 compared to 1 KeV to 2.5 KeV in U-238).

The values of the resolved contribution to the resonance integral are given in Table 4A. They show the required increase with increasing temperature (see Eq. 18). Effective resonance integrals for  $T = 300^{\circ}\text{K}$  as calculated by the HRG-program are plotted against  $\sigma_s^*$  in Fig. 2.

Because of the lack of measurements of the effective U-235 resonance integral for finite dilution no comparison with experiments can be made, however, it is possible to compare the effective fission integral for infinite dilution with the calculated value. As shown later in Sec. 3.4 the agreement with experiment is excellent.

### 3.3 Revision of HRG-Program

In the two preceding sections it was shown that the calculation of the unresolved resonance integrals for higher temperatures is erroneous.

In order to understand the approximation used, the relevant points leading to this approximation will be summarized:

1. Both with increasing temperature and with increasing dilution the effective resonance integral tends to an asymptotic value. This asymptotic value is for both cases the infinite dilution integral because the latter is temperature independent.

2. For high temperatures and energies  $> 20$  eV the Doppler width tends to be in the order of the average level spacing (see Tables 1 and 2), where the Doppler width is the width at which the cross section has approximately a value one-half of that at the resonance peak.

Thus in the considered range of energies and temperatures the broadening of the resonances is essentially an "averaging process" for the resonance cross sections over the entire energy range.

The following conclusion can be drawn from the second point: For temperatures larger than approximately  $2000^{\circ}\text{K}$  the unresolved resonance integral is temperature independent.

The problem now is to calculate this temperature independent part of the total resonance integral by means other than the finite difference approximation of the unresolved resonance formula (10).

This can be accomplished according to the above mentioned first point by replacing the temperature independent unresolved part for this energy range by the infinite dilution integral which is also temperature independent.

Obviously a further requirement is that the dilutions for the cases considered (i.e., for gaseous core reactors) are large enough, i.e., already within the asymptotic resonance integral range. Fortunately this is the case because for gaseous reactors  $\sigma_s^*$  lies in the order of  $10^4$ , i.e., within the asymptotic range (see Fig. 2).

Thus the resonance integrals for higher temperatures and for  $\sigma_s^*$  in the neighborhood of  $10^4$  are calculated by adding the constant value for the infinite dilution integral to the contributions of the resolved resonances.

The following revisions of the HRG-program are made:

1. Because the calculation of the unresolved resonance integral for  $T = 300^\circ\text{K}$  can be considered as correct (see following comparison with experiments) this "virtual" temperature was built into the program for the unresolved resonance calculations for temperatures larger than  $2000^\circ\text{K}$ .

2. To obtain the infinite dilution integral, the input parameter  $\sigma_{m(\text{eff})}$  (= effective cross section for unresolved resonance calculation) is given as  $10^8$ . Figure 2 shows that this value is large enough to give the infinite dilution integral.

3. The capture and absorption cross sections in the unresolved region were taken from Ref. 9 ( $\sigma_f$ ) and Ref. 10 ( $\sigma_{n,\gamma}$ ) and built into the program. This leads to a correction factor of + 1.06295 for the absorption integral and + 1.03029 for the fission integral. These cross sections are listed in Table 5.

#### 3.4 Resonance Integrals for U-235 by Revised HRG-Program and Comparison with Experimental Results

The effective resonance integrals calculated by the revised HRG-program are listed in Tables 6A and 6B. The unresolved resonance integrals for  $T = 300^\circ\text{K}$  and  $\sigma_s^* = 10^8$ ,  $T = 10.000^\circ\text{K}$ , and  $T = 40.000^\circ\text{K}$  show all the same value which are the infinite dilution integrals for this region. Table 6B, which contains the sum of both the resolved and the unresolved contribution of the effective resonance integral, shows the required increase with increasing dilution and temperature.

It is possible to compare the effective fission integral for infinite dilution with experiments. As reported in Ref. 8, the measured integral is 271 barns from the 0.49 eV - cadmium cut-off. It can be assumed that this value is valid for the whole energy range because the contributions from a negative resonance and the resonance at 0.29 eV are canceled approximately by the cross section deficit between 0.29 eV and the cadmium cut-off where the cross section decreases faster than  $1/v$ .

The calculated infinite dilution integral for fission between 1.125 eV and 3.36 KeV is 200.33 barns (see Table 6B for  $T = 300^\circ\text{K}$ ). The following contributions must be added (the cross sections are obtained from Ref. 9 and HRG-program library data):

$E_{\min}$	$E_{\max}$	$\overline{\sigma}_f$	$\Delta u$	$I_f$
3.36 KeV	10 MeV	2.15	8.0	17.2
1.125 eV	3.36 KeV	—	—	200.33
0.876	1.125	72.0	0.25	18.0
0.683	0.876	55.2	0.25	13.8
0.532	0.683	65.1	0.25	16.3
0.490	0.532	74.0	0.082	6.1
total:				271.73

This value compares favorably with the measured one.

source	measured*	calculated*		rev. HRG-program
		I	II	
$I_{\text{eff}}$ (barns)	271.	260.	255.	271.7

\* From Ref. 8: I = estimated from average level parameters  
 II = for  $1/v$  cross section



#### 4. U-235 RESONANCE CROSS SECTION CALCULATION

##### 4.1 Selection of Gaseous Core Reference System

In order to reduce the set of parameters affecting the final resonance cross sections by two, a gaseous core reference system is defined. The system is selected by the criterion that it shall be representative and typical with respect to the two parameters for all gaseous core reactor designs possible. The two parameters are dilution and geometric buckling, the first being a measure for the amount of scattering material present and the second being a quantity related to the size of the reactor.

1. dilution, i.e., scattering cross per absorber atom  $\sigma_s^*$ . For all gaseous core reactor systems this value lies in the order of  $10^4$  and higher. From Fig. 2 it can be concluded that the cross sections in this range have reached an asymptotic value, i.e., they are only slightly changing for increasing  $\sigma_s^*$ .

Two values of  $\sigma_s^*$  were selected:

$$\sigma_s^* = 10^4$$

$$\sigma_s^* = 0.5 \times 10^4 .$$

The second value was chosen to cover the range of experimental results, where highly enriched uranium in the form of thin foils was used to approximate a gaseous uranium filling (see Sec. 5.3).

2. buckling, i.e., the size of the gaseous core reference system. This quantity had to be chosen in a more

arbitrary fashion, although an upper and lower limit on the buckling can be established.

An upper limit on the geometric buckling, i.e., a lower limit on the dimensions, is given by the calculational method used in the HRG-program. For smaller reactors (i.e., radii in the order of cm) the  $B_1$ -approximation is not sufficient to treat the energy-angle dependence of the neutron flux and higher order  $B_n$ - or  $S_n$ -methods are necessary.

An upper limit on the reactor dimension can be set by practical considerations. Because this reactor concept is considered primarily for use in propulsion devices, a natural upper limit is given by its weight. In general, radii in excess of 2 meters are very unlikely for practical purposes.

The chosen value for the buckling,  $B = 0.0225$ ,\* corresponds to an optimum value reported in previous calculations (see Ref. 1 and Ref. 2). However, in order to visualize the influence of the buckling on slowing down flux and cross sections, some calculations were performed for two other values of  $B$  (see Sec. 4.3).

#### 4.2 Final Cross Section Calculations and Comparison with LASL-6- and 16-Group Cross Sections

The calculated effective resonance cross sections for a temperature range  $300 - 40.000^\circ\text{K}$  and the two chosen values for  $\sigma_s^*$  are listed in Table 7. The cross sections were averaged over the slowing down flux corresponding to the "reference buckling"  $B = 0.0225$ . The scattering matrices are not given because they correspond exactly to the values of the LASL-16

---

\* For example, critical sphere with cavity radius = 80 cm; reflector thickness = 100 cm; cavity with  $n_u \approx 1.3 \times 10 \text{ at/cm}^3$ ;  $n_H \approx 1.3 \times 10^{19} \text{ at/cm}^3$ ; reflector = graphite; overall temperature =  $300^\circ\text{K}$ .

group and showed a negligible change ( $4^{\text{th}}$  significant figure) with temperature and the considered dilutions.\*

Some trends shall be pointed out. The maximum change for a particular cross section occurs between  $300^{\circ}\text{K}$  and  $2320^{\circ}\text{K}$ , corresponding to the steep increase of the resonance integrals in this temperature range. For higher temperatures the difference becomes smaller.

Within the group structure, groups 10 and 11 (upper resolved resonances) show the largest differences for increasing temperature or dilution indicating the strong influence of the Doppler effect on this range.

The two sets with which the calculated cross sections shall be compared are the LASL-6 group set and the LASL-16 group set, the first being a fast detector cross section set and the second being a set which was prepared for calculations of homogeneous epithermal systems. These are compared with cross sections determined for a system which is almost to 100 per cent thermal<sup>1,12,13,16,18,\*\*</sup>. Therefore not too much physical insight can be expected from the comparison, i.e., the question reduces more or less to an "order-of-magnitude" analysis. Nevertheless, I should like to point out that a "disguised" integral comparison is made in Sec. 5.3 where measured critical masses are compared with calculated ones.

---

\* For example, for group 9 ( $30 \div 100 \text{ eV}$ ) and  $\sigma_s^* = 10^4$

$\sigma$	LASL	HRG	
		$T = 300^{\circ}\text{K}$	$T = 40.000^{\circ}\text{K}$
$\sigma_{i \rightarrow i+1}$	0.05	0.049(899)	0.049(868)

\*\* That a gaseous core reactor is almost completely thermal can also be concluded from the extremely high  $\sigma_s^*$

The comparison is restricted to capture and fission cross sections. For the LASL-6 group set also the transport cross section shall be compared.

Table 8A gives the values for 6 energy groups. The LASL-6 group cross sections for energy group 6 (0.414 eV ÷ 0.1 MeV) were obtained by weighting the relevant LASL-16 group cross sections over an 1/E - spectrum; according to:

$$\bar{\sigma} = \frac{\int_{0.414 \text{ eV}}^{0.1 \text{ MeV}} \sigma \, dE/E}{\int_{0.414 \text{ eV}}^{0.1 \text{ MeV}} dE/E} \quad (21)$$

In the upper five energy groups the calculated cross sections\* are larger than the LASL-6 group values. This is due to the fact that the LASL-6 group cross sections are weighted over a fission spectrum, whereas the HRG-values are weighted over the slowing down flux in this energy range.

For group 6 the situation is reversed. Here the LASL-values are larger. This must be due to the artificial weighting corresponding to Eq. 21 which introduces, at least for energies near thermal, weighting errors. Still there are no alarming large differences, considering the fact that the compared systems are quite different.

Table 8B compares the values for the 16-group cross section set. It indicates a certain cross section shift for the calculated values. The values for energy groups 8, 9, 10, 12 are smaller than the corresponding LASL-cross section, whereas groups 11 and 13 show higher values. A possible ex-

---

\* By HRG-program for  $T = 300^{\circ}\text{K}$ ; gaseous core "reference system."

planation for this behavior is the calculational method inherent in the HRG-program. There are indications which are, unfortunately, very tedious to check, that the HRG-group structure ( $\Delta u = 0.25$  throughout) compresses closely spaced resonances into one particular group although a main part of one of the resonances affects the groups lower or higher in energy. Thus, some groups have a higher "importance" than others. Although there are considerable differences between the LASL - and HRG-values, there exists strong evidence\* that they are comparable if applied to specific reactor systems. This evidence is given by the comparative analysis performed in Sec. 5.3 where measured critical masses are compared with critical masses calculated by the LASL-16 group and varied LASL-16 group (resonance cross sections changed). The calculated masses differ by 10 - 20 per cent, where the HRG-values lie closer to the measured critical masses than the LASL-values.

#### 4.3 Effect of Buckling and Dilution on Slowing Down Flux

In this section the well-known effects of buckling and dilution (being in this connection a measure of the scatterer-to-absorber-atomic ratio) on the slowing down flux and thus on the resonance cross sections which are averaged over this flux are investigated. The buckling determines together with slowing down length and age the thermal and fast leakage from the system whereas the dilution affects the probability of fission neutrons to be slowed down to thermal energy. A higher dilution results in a higher slowing down probability,

---

\* Another evidence, not so convincing, is given by the fact that the average cross sections over the resonance region are not too different (see preceding comparison with LASL-6 group).

whereas small dilutions result in flux distributions which are peaked at higher energies.

1. dilution: Figure 3 shows two slowing down fluxes (per unit lethargy) for two dilutions differing by a factor of 100. The value for  $\sigma_s^* = 110.75$  corresponds to a graphite-uranium system with  $C/U = 21$ . The usual (see Ref. 3) steep decrease with increasing lethargy in the epithermal region can be observed. Table 9 gives the resonance cross sections averaged over this spectrum. As can be expected they differ extremely from LASL-16 group values. The "gaseous core reference system"  $\sigma_s^* = 10^4$  shows an extremely different flux behavior. The epithermal flux behaves nearly as  $1/E$  in the epithermal region, which essentially provides the background for the cross section comparison in the preceding section.

2. buckling: Figure 4 shows the slowing down flux for the gaseous core reference system at  $T = 40.000^\circ\text{K}$  and the buckling as parameter. The range of the selected buckling values is the range mentioned in Sec. 4.1. The three bucklings  $B = 0.01; 0.02245; 0.045$ ; correspond (for a spherical gaseous core reactor system) to radii of approximately  $r_c \cong 2\text{m}; 80\text{ cm}; 30\text{ cm};^*$  thus covering the abovementioned relevant range. Because all three curves are normalized to the same factor only a relative comparison is possible. The largest sphere has the highest thermal flux and the smallest fast leakage, whereas the sphere with approximately 30 cm core radius has a higher fast leakage than the two spheres with larger core radii. The largest relative difference from the "average" buckling  $B = 0.02245$  is approximately 15 per

---

\* For a graphite reflector of 1m thickness.

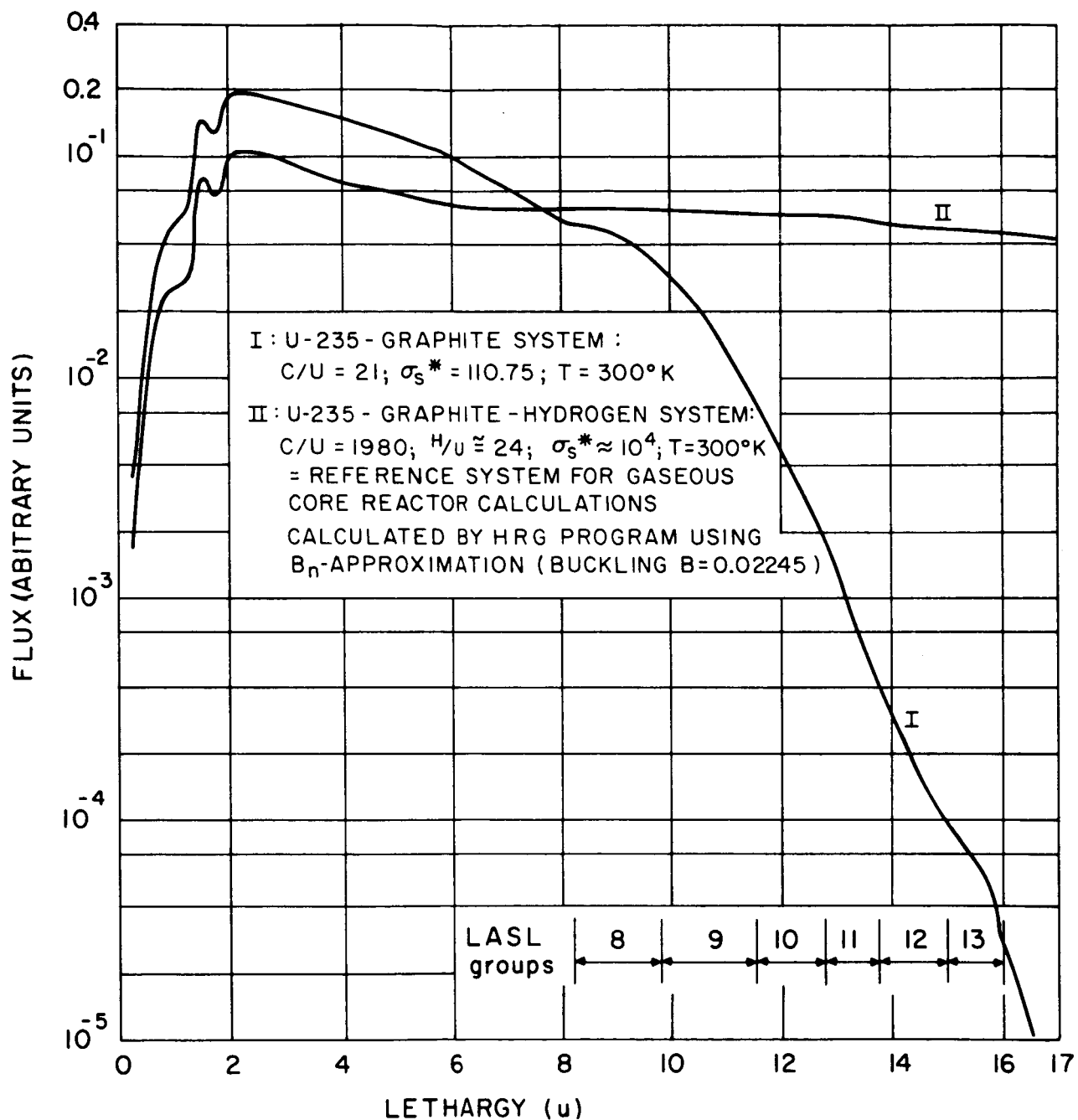


FIG. 3 SLOWING DOWN FLUX FOR VARIOUS DILUTIONS

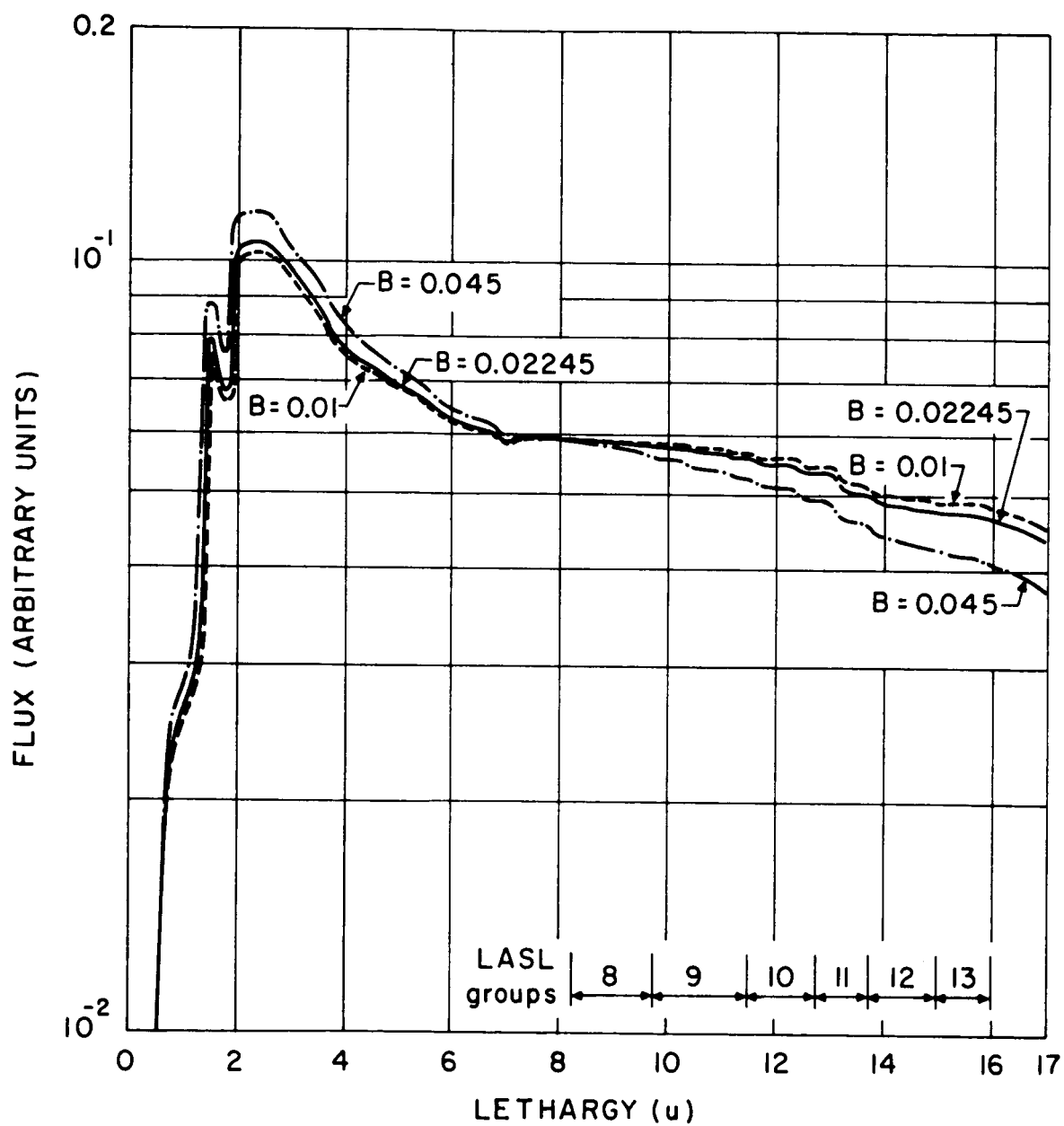


FIG. 4 SLOWING DOWN FLUX FOR VARIOUS BUCKLINGS  
 (FOR GASEOUS CORE REFERENCE SYSTEM)  
 $B_1$  - APPROXIMATION;  $T = 40,000^\circ\text{K}$



cent ( $u > 17.0$ ), but the effect on the resonance cross section weighted by these spectra is much smaller ( $\approx .4\%$  for  $\sigma_{n,\gamma}$ ). Table 9 compares the weighted cross sections corresponding to these spectra together with cross sections weighted over a  $1/E$ -spectrum.

For the whole resonance range the relative differences from  $B = 0.02245$  never exceed an error of  $\pm .4$  per cent. Thus the error introduced by varying the buckling lies in the range of errors inherent in the measurements of the basic cross sections. Even cross sections averaged over an  $1/E$  spectrum differ at the most by approximately 1 per cent thus verifying the statement previously made that the slowing down flux in the epithermal region in a gaseous core reactor can be considered\* as rather close to the asymptotic spectrum. It can be concluded that differences in the resonance cross sections resulting from a buckling variation within the above-mentioned limits can be neglected.

#### 4.4 Estimate of Doppler Coefficient of Reactivity

In the following section (5) three main parameters shall be investigated, two of which have already been mentioned, i.e., the investigation of the homogenization assumption used in the calculation of the effective resonance integrals and secondly the comparison with measured and previously calculated critical masses. A third, rather stringent condition concerns the Doppler coefficient of reactivity. It is possible to evaluate the Doppler coefficient using the calculated resonance integrals. The resonance escape probability for a homogeneous mixture of scatterer and absorber is given by:

$$p = \exp\left[-\frac{1}{\xi\Sigma_s} \int_E^{E_c} \frac{\Sigma_a}{1 + \Sigma_a/\Sigma_s} \frac{dE'}{E'}\right] \quad (22)$$

---

\* With respect to the weighting of resonance cross sections.

With the previously defined effective resonance integral one obtains:

$$p = \exp\left(-\frac{N_u}{\xi \sigma_s} I_{\text{eff}}\right)$$

or

$$p = e^{-\frac{I_{\text{eff}}}{\bar{\xi} \sigma_s^*}} \quad (\text{for mixtures}) \quad (22a)$$

where  $\bar{\xi}$  is defined by:

$$\bar{\xi} = \frac{\sum_i \xi_i \sigma_{si}}{\sum_i \sigma_{si}} = \frac{\sum_i \xi_i \sigma_{si}^*}{\sum_i \sigma_{si}^*} \quad (23)$$

Then:

$$\frac{1}{p} \frac{dp}{dT} = -\frac{1}{\bar{\xi} \sigma_s^*} \frac{dI_{\text{eff}}}{dT} \quad (24)$$

The Doppler coefficient of reactivity is defined by:

$$\left. \frac{dk}{dT} \right|_{\text{Doppler}} = \frac{1}{p} \frac{dp}{dT} \quad (25)$$

It follows from Eqs. 23, 24 and 25 that:

$$\left. \frac{dk}{dT} \right|_{\text{Doppler}} = -\frac{1}{\sum_i \xi_i \sigma_{si}^*} \frac{dI_{\text{eff}}}{dT} \quad (26)$$

The stringent conditions imposed upon the calculations for a realistic reactor system shall be that the Doppler coefficients calculated for the idealized "gaseous core reference system" by the HRG-program must be the same (or at least lie in reasonable limits) as those determined for a realistic gaseous core reactor system using the calculated resonance cross sections. This statement will be examined in Sec. 5.2.

Selected "gaseous core reference system"

$$n_H = 1.3 \times 10^{19} \text{ atoms/cm}^3$$

$$n_U = 1.3 \times 10^{19} \text{ atoms/cm}^3$$

$$n_C = 8.38 \times 10^{22} \text{ atoms/cm}^3$$

This corresponds to  $\sigma_s^* \approx 10^5$ . This system can be assumed to be representative for all the major gaseous core reactor systems because the reactivity-change varies only slightly with  $\sigma_s^*$  in the range from  $0.5 \times 10^4$  to  $10^5$ . The following effective resonance integrals and  $\Delta k$  ( $\Delta k = \frac{dk}{dT} \cdot \Delta T$ ) Doppler

were determined using the  $\sigma_s^* = 10^4$  - set of resonance cross sections (see Table 7).

Temp. [°K]	300	2320	5800	10.000	40.000
$I_{abs}[b]$	316.65	327.76	328.23	328.44	328.39
$I_{fiss}[b]$	195.58	199.42	199.67	199.79	199.82
$\Delta k$	-0.00104		-0.00006*		

\* Only one value was determined between  $T = 2320^\circ\text{K}$  and  $T = 40.000^\circ\text{K}$  because of the flat, almost linear, change in the effective resonance integral.

The extremely small reactivity change due to Doppler broadening between  $T = 2320^\circ\text{K}$  and  $40.000^\circ\text{K}$  is negligible even for very refined reactor calculations. However, the reactivity change up to  $T = 2320^\circ\text{K}$  has to be taken into account.

## 5. APPLICATION TO SPECIFIC GASEOUS CORE REACTOR SYSTEMS

The critical masses quoted in this section were determined using the CRAM-program<sup>11</sup>, a multigroup diffusion program. Sixteen energy groups, with group boundaries corresponding to the LASL-cross section set, were taken to represent the slowing down flux. In order to introduce the calculated resonance cross sections the corresponding LASL-cross sections in the CRAM-program library were changed in the input data. In the following tables the corrected LASL-cross sections, i.e., corrected in the resonance region, are designated "HRG", referring to the program which was used to compute these cross sections.

Two preliminary computations were performed in order to determine the cavity radius corresponding to the minimum critical mass and secondly to check space-differencing errors introduced by the finite spatial mesh width.

The following results were obtained for the cavity radius calculation:\*

- Data:
1. cavity is homogeneously filled with gaseous uranium and hydrogen having approximately equal atomic densities.
  2. graphite reflector with thickness = 100 cm and atomic density =  $8.38 \times 10^{22}$  at/cm<sup>3</sup>.
  3. HRG-resonance cross sections ( $T = 300^{\circ}\text{K}$ ).

---

\* All critical data, except those for the recalculation of the cylindrical experiments, were obtained for spherical systems.

Cavity radius [cm]	mesh width in cavity [cm]	$n_H$ [at/cm <sup>3</sup> ]	$n_U$ [at/cm <sup>3</sup> ]	$n_H/n_U$	$m_{cr}$ [kg]
40	0.5	$1.52 \times 10^{20}$	$4.545 \times 10^{20}$	0.335	47.5
60	0.75	$2.845 \times 10^{19}$	$4.62 \times 10^{19}$	0.616	16.3
80	1.25	$1.703 \times 10^{19}$	$1.137 \times 10^{19}$	1.5	9.51
100	1.25	$1.297 \times 10^{19}$	$6.46 \times 10^{18}$	2.01	10.55
150	1.875	$4.81 \times 10^{18}$	$2.63 \times 10^{18}$	1.9	14.92

Figure 5 gives a plot of  $m_{cr}$  versus the cavity radius indicating a minimum critical mass for a cavity radius of 80 cm. This radius was selected for all the following computations.

The checking calculations with respect to the space-differencing-error gave the following results (See Fig. 6):

- data: 1. reflector thickness: 100 cm  
2. graphite atomic density:  $n_c = 8.38 \times 10^{22}$  at/cm<sup>3</sup>  
3. hydrogen atomic density within homogeneously filled cavity:  $n_H \approx 1.0 \times 10^{19}$  at/cm<sup>3</sup>  
4. LASL-16 group cross sections

mesh width in cavity [cm]	8	4	2	1.75	1.25	1
$m_{cr}$ [kg]	18.15	9.9	8.3	9.24	9.39	9.3

All the following results were determined using the asymptotic spacing of approximately 1.25 cm. For not comparable calculations, e.g., for cylinders or "experimental" spheres, this rather time consuming check with respect to mesh width was repeated.

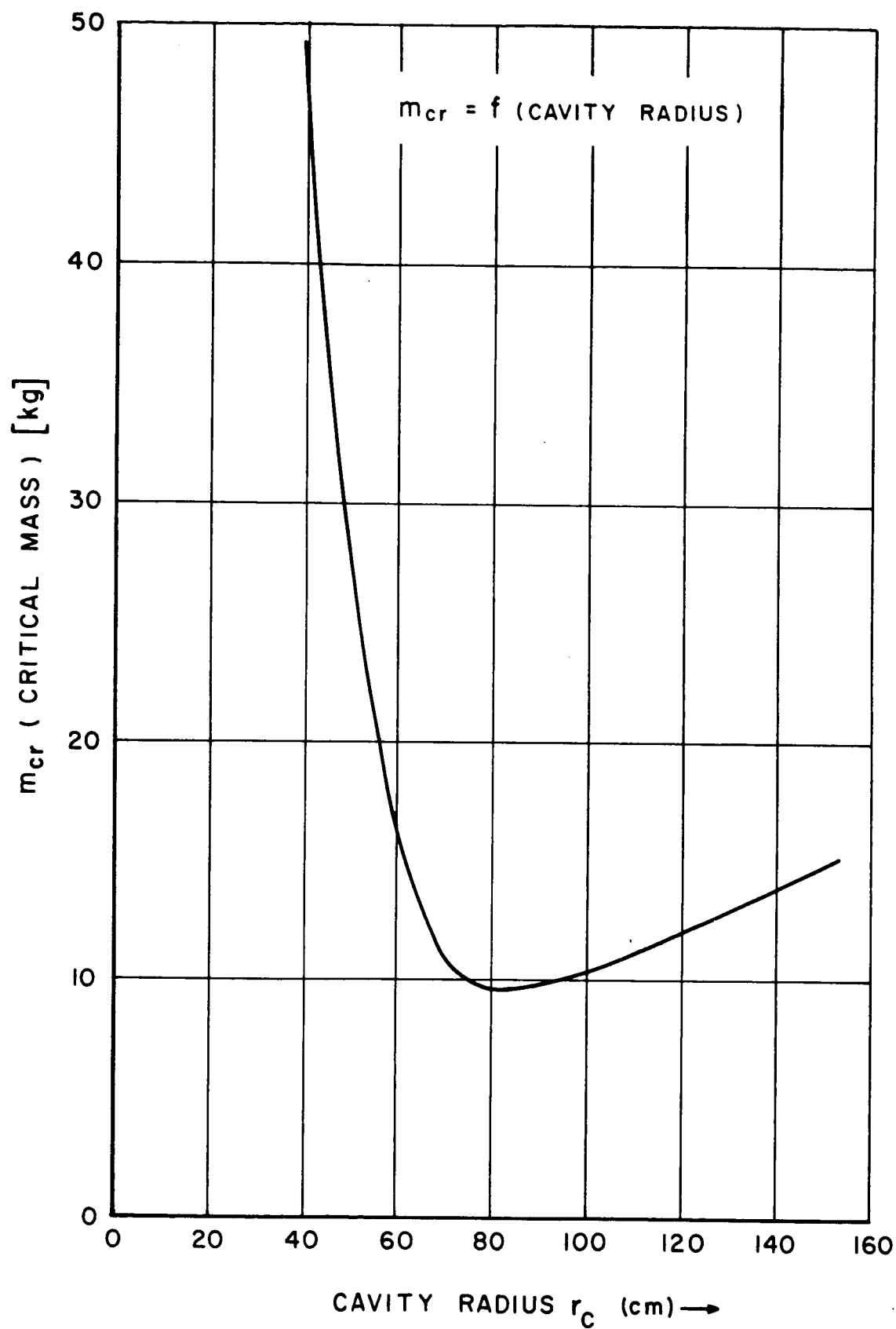


FIG. 5 HOMOGENEOUS CAVITY WITH  $n_H \approx n_U$   
100 cm GRAPHITE REFLECTOR

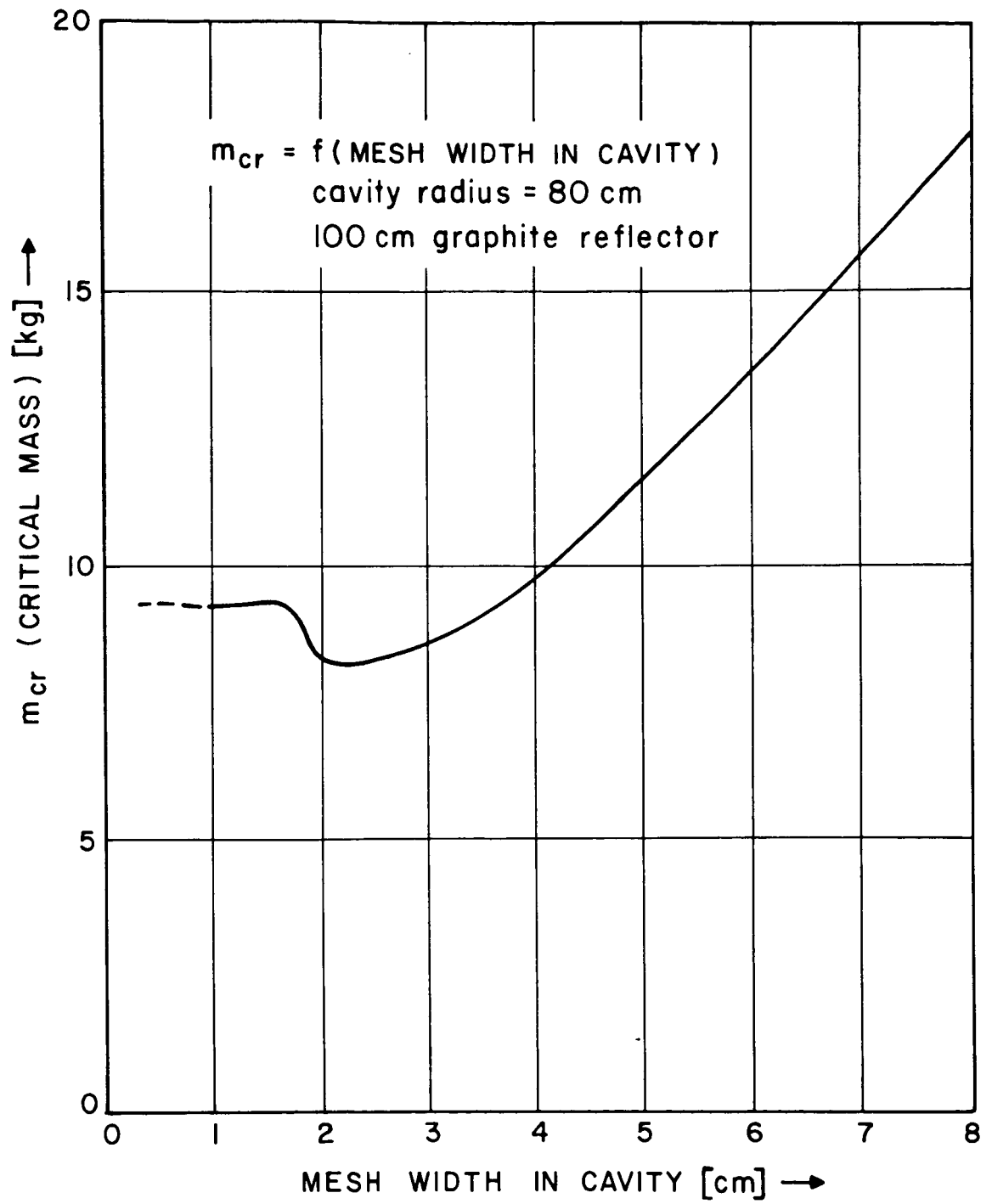


FIG. 6

## 5.1 Check of Homogenization Assumption and Comparison With Previous Theoretical Results

### 5.1.1 Comparison With Calculated Critical Masses

At least two main parameters, i.e., the presence of hydrogen in the cavity and the reflector atomic density, enter the calculation of the critical mass. Therefore, the data presented in this section are divided into two parts. Furthermore, it shall be noted that the critical masses are calculated for a homogeneous filling of the cavity. Heterogeneous effects are discussed in Sec. 5.4.

#### a. Cavity without hydrogen

Data:  $r_{\text{cav}} = 80 \text{ cm}$ ;  $r_{\text{total}} = 180 \text{ cm}$   
 reflector = graphite  
 fuel-and reflector temperature =  $300^\circ\text{K}$

TABLE A

Case	Ref.	Method	Resonance x-sections	Reflector dens. [at/cm <sup>3</sup> ]	U-235 dens. [at/cm <sup>3</sup> ]	$m_{\text{cr}}$ [kg]
A1	Safonov <sup>13</sup>	age		*	$3.34 \times 10^{19}$	28
A2	Mills <sup>12</sup>	SNG	LASL	*	$1.242 \times 10^{19}$	10.4
A3	Holl <sup>1</sup>	Diffusion	LASL	*	$1.67 \times 10^{19}$	14
A4	author	Diffusion (CRAM)	LASL	$8.38 \times 10^{22}$	$1.101 \times 10^{19}$	9.21
A5	author	Diffusion (CRAM)	LASL	$7.54 \times 10^{22}$	$1.757 \times 10^{19}$	14.7
A6	author	Diffusion (CRAM)	HRG	$8.38 \times 10^{22}$	$1.1293 \times 10^{19}$	9.45
A7	author	Diffusion (CRAM)	HRG	$7.54 \times 10^{22}$	$1.811 \times 10^{19}$	15.15

---

\* Not known.



Unfortunately a direct comparison of previous results with the cases A4 to A7 is not possible because of the different methods employed, the unknown graphite density in the previous calculations, and the different mesh widths used. The determined critical masses fluctuate, depending on the above parameters, between 10 and 17 kg. One conclusion, however, is possible, i.e., age theory overestimates the required critical mass considerably.

Because of the above reasons the discussion shall be restricted to cases A4 to A6. A first conclusion is that the calculations using the revised resonance cross sections give a higher critical mass ( $2 \div 4$  per cent depending on the specific case) than the "pure" LASL-cross sections. This fact will be of importance for the recalculation of measured critical masses presented in Sec. 5.3.

Secondly a decrease in graphite density increases the critical mass, e.g., a decrease of the graphite density by 10 per cent increases the critical mass by  $\sim 70$  per cent. Thus reflector temperature effects will be of great importance in gaseous core reactors. This temperature problem involving the calculation of thermal cross sections is the subject of a later report.

b. Cavity with hydrogen

Data: same data as in table A;

$$\text{graphite atomic density } n_C = 8.38 \times 10^{22} \text{ at/cm}^3$$

Figure 7 shows a plot of  $m_{cr}$  versus the hydrogen-to-uranium-atomic ratio within the cavity. The presence of hydrogen (for  $n_H/n_U > 2$ ) is seen to decrease the critical mass considerably due to the increasing slowing down power of the cavity. This behavior, however, is merely of theoretical interest because in the actual considered gaseous core reactor devices

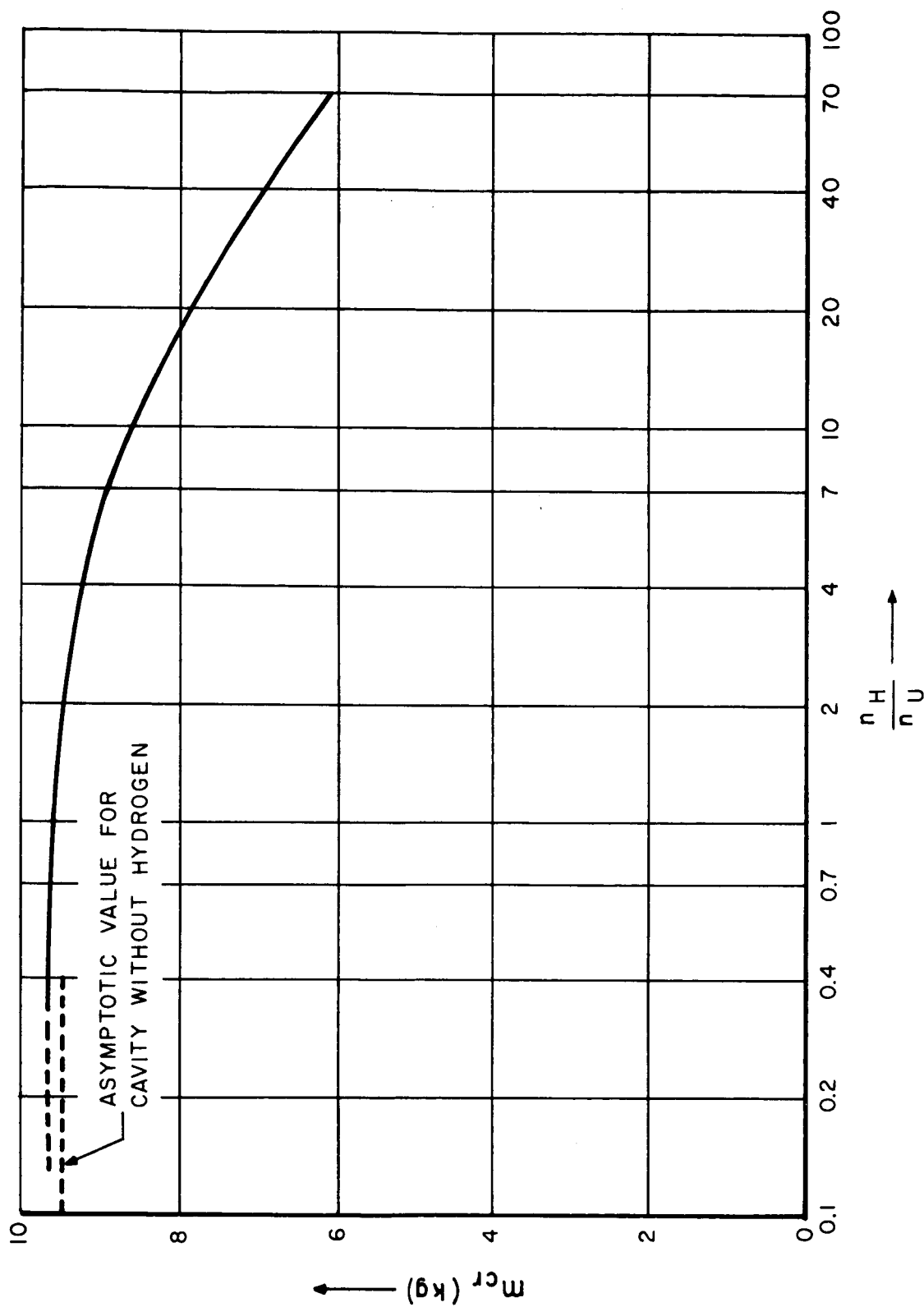


FIG. 7  $m_{cr} = f\left(\frac{n_H}{n_U} \text{ IN CAVITY }\right)$

TABLE B

case	res. cross sect.	$n_U$ [at/cm <sup>3</sup> ]	$n_H$ [at/cm <sup>3</sup> ]	$n_H/n_U$   cavity	$m_{cr}$ [kg]
B1	HRG	$1.150 \times 10^{19}$	$3.456 \times 10^{18}$	0.301	9.62
B2	HRG	$1.137 \times 10^{19}$	$1.703 \times 10^{19}$	1.50	9.51
B3	HRG	$1.124 \times 10^{19}$	$2.302 \times 10^{19}$	2.05	9.40
B4	HRG	$1.030 \times 10^{19}$	$1.030 \times 10^{20}$	10.	8.62
B5	HRG	$8.570 \times 10^{18}$	$3.059 \times 10^{20}$	35.7	7.17
B6	HRG	$7.898 \times 10^{18}$	$4.230 \times 10^{20}$	53.6	6.61
B7	HRG	$7.504 \times 10^{18}$	$5.086 \times 10^{20}$	67.8	6.28
B8	HRG	$7.441 \times 10^{18}$	$5.237 \times 10^{20}$	70.4	6.23
B1*	LASL	$1.1224 \times 10^{19}$	$3.558 \times 10^{18}$	0.32	9.39
B2*	LASL	$1.1114 \times 10^{19}$	$1.7478 \times 10^{19}$	1.57	9.30

uranium and hydrogen are separated and the influence of hydrogen is modified, although still of extreme importance, depending on the actual type of gaseous core reactor considered. Some remarks in this respect are made in Sec. 5.4, but a complete evaluation of this problem is left to a later report.

A rather intriguing behavior is encountered for very low  $n_H/n_U$ -ratios. There the required critical mass is seen to be larger than the asymptotic value, i.e., for a cavity without any hydrogen present. It drops below this value for  $n_H/n_U$ -ratios greater than 2. Some checking calculations (not given in Table B) showed that a further decrease of  $n_H/n_U$  below 0.30 (see case B1) resulted in critical masses going asymptotically toward the critical mass for the cavity without hydrogen.

A possible explanation for this behavior is that for very low  $n_H/n_U$ - ratios neutrons within the cavity having energies above thermal are not affected by the presence of hydrogen whereas thermal neutrons entering the cavity from the reflector can be scattered back into the reflector. This might be an explanation for the lower thermal flux within the cavity of case B1 as compared to the thermal flux of case A6, both shown in Fig. 8. If the  $n_H/n_U$ - ratio increases the scattering probability for high energy neutrons within the cavity increases also. This results in higher thermal flux within the cavity and the fuel is better utilized.

The two starred cases at the end of Table B are calculated using the "pure" LASL-16 group set. Compared with the unstarred cases B1 and B2 the results again show higher critical masses for cases calculated with the HRG-resonance cross sections.

#### 5.1.2 Homogenization Assumption (Spatial Dependence)

In Sec. 2.1.a,I made the assumption that the surface term of the effective resonance integral can be neglected due to the large neutron mean free path in the cavity. The resonance integral was determined for a homogeneous mixture of scatterer and absorber. In order to clarify the pattern of the following discussion the two successive steps in calculating the resonance cross sections shall be repeated:

1. First the effective absorption and fission resonance integrals were determined. Here it was assumed that the mixture (consisting of uranium, hydrogen and graphite atoms) is homogeneous. This question concerning the spatial dependence of the slowing down flux shall be examined in this section.
2. To obtain the resonance cross sections, the resonance integrals of a particular group were weighted over the slowing down flux corresponding to the idealized

CASE A6 :  $n_U = 1.129 \times 10^{19} \text{ at/cm}^3$  ;  $n_H = 0$   
 CASE B1 :  $n_U = 1.150 \times 10^{19} \text{ at/cm}^3$  ;  $n_H = 3.5 \times 10^{18} \text{ at/cm}^3$   
 CASE B8 :  $n_U = 7.441 \times 10^{18} \text{ at/cm}^3$  ;  $n_H = 5.2 \times 10^{20} \text{ at/cm}^3$   
 (REFLECTOR = GRAPHITE ;  $n_C = 8.38 \times 10^{22} \text{ at/cm}^3$ )

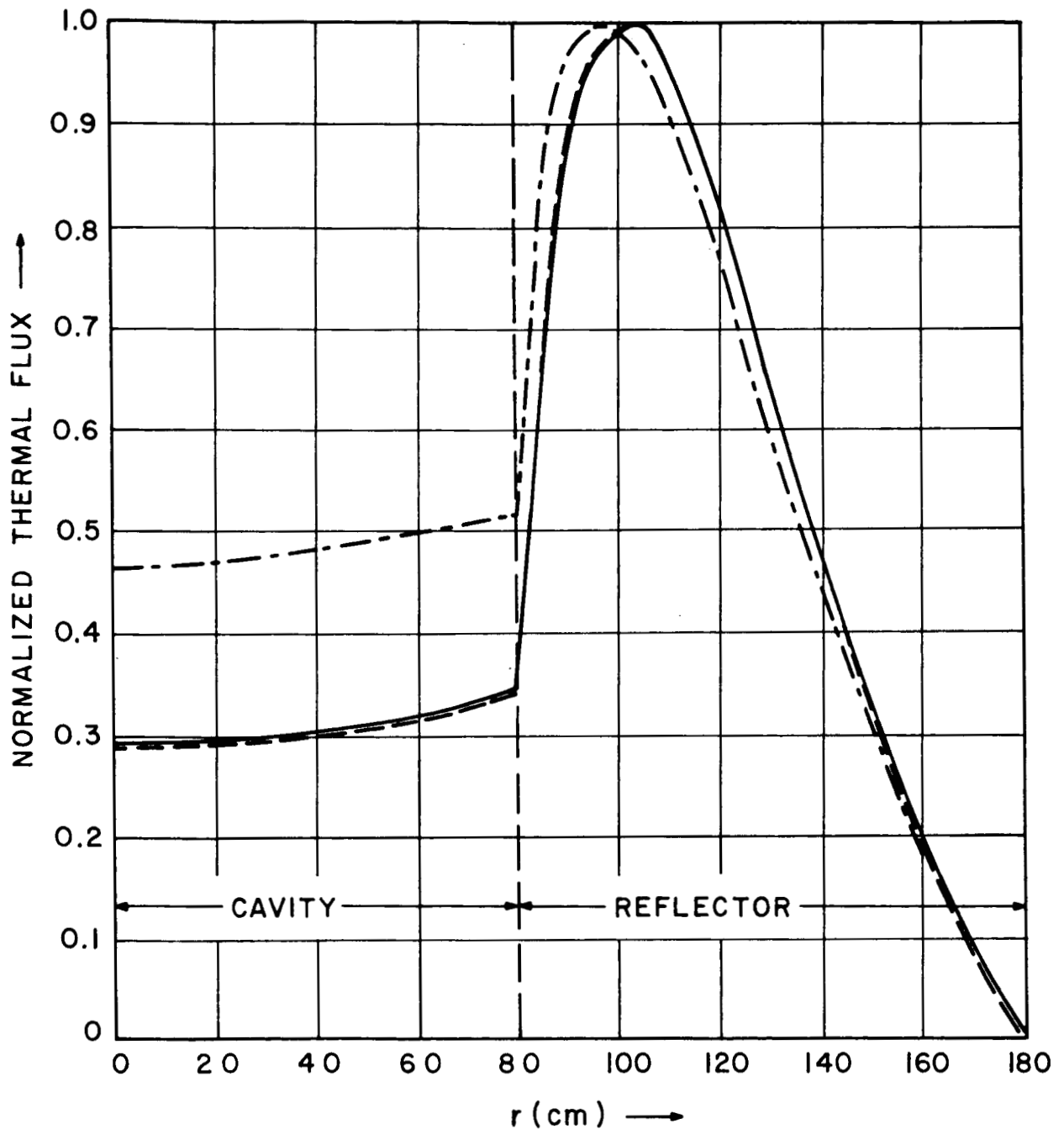


FIG. 8 RADIAL DEPENDENCE OF THERMAL FLUX .

(i.e. homogeneous) "gaseous core reference system" with an averaged value for the buckling. This energy dependence of the slowing down flux shall be investigated in Sec. 5.1.3.

The discussion of the spatial dependence can be restricted to the following ranges: (a) only the resonance fluxes and (b) their behavior in the central cavity are of interest.

In order to verify the assumption in Sec. 2.1.a, it has to be shown that the mean free path of neutrons within the cavity is very large or, expressed in another way, that the absorption probability for neutrons with energies between 1ev and 3Kev (= resonance region) is very low. Thus I want to investigate what can be called the "cavity self shielding".

Table 10 lists the resonance fluxes as function of cavity radius for case A6, i.e., for a cavity of 80 cm radius filled with gaseous uranium and reflected by 100 cm graphite.

The flux values (arbitrary units) show that the flux depression within the cavity can be entirely neglected because the differences occur in the fourth or fifth significant figure. This essentially means that neutrons traverse the cavity without "feeling" the presence of uranium.

It was shown in Table B that the presence of hydrogen within the cavity had an extreme influence on the required critical mass. Of interest here is the influence of hydrogen on the shape of the cavity resonance flux. The following table compares three cases:

case	$n_H/n_U$	flux			
		resonance group 8		resonance group 12	
		$r = 0.625 \text{ cm}$	$r = 79.375 \text{ cm}$	$r = 0.625 \text{ cm}$	$r = 79.375 \text{ cm}$
A6	0.	82538.	82542.	37644.	37701.
B2	1.5	82505.	82511.	37811.	37875.
B8	70.	65341.	65311.	35684.	35664.

The table shows that the absolute magnitude of the resonance fluxes decreases with increasing hydrogen content; however, the spatial variations of the fluxes over the cavity are insignificant.

The above results show that the behavior of the slowing down flux in the resonance region with respect to its spatial dependence verifies the first part of the homogenization assumption which stated that spatial resonance flux variations can be neglected.

At this point a sidestep shall be taken in order to show the influence of hydrogen on the thermal flux across the spherical reactor. Figure 8 gives a plot of the calculated thermal flux versus the reactor radius for cases A6, B1, and B6. Obviously the presence of hydrogen influences the thermal flux within the cavity considerably. The shape is not changed but the absolute magnitude is increased with increasing hydrogen content, i.e., for higher  $n_H/n_U$ -ratios the cavity acts as an added slowing down region. The decrease in thermal flux for very low  $n_H/n_U$ -ratios (case B1) was already mentioned in the discussion of table B and Fig. 7.

#### 5.1.3. Energy Dependence of Slowing Down Flux

The second part of the homogenization assumption, i.e. the question in connection with the cross section weighting spectrum, does not show the same excellent agreement with the actual reactor case as does the first part.

Figure 9 shows two slowing down fluxes as function of lethargy. The first corresponds to the "gaseous core reference system" as calculated for a homogeneous mixture of scatterer and absorber by the HRG-program. The second curve shows the approximated (16 groups) slowing down flux calculated by the

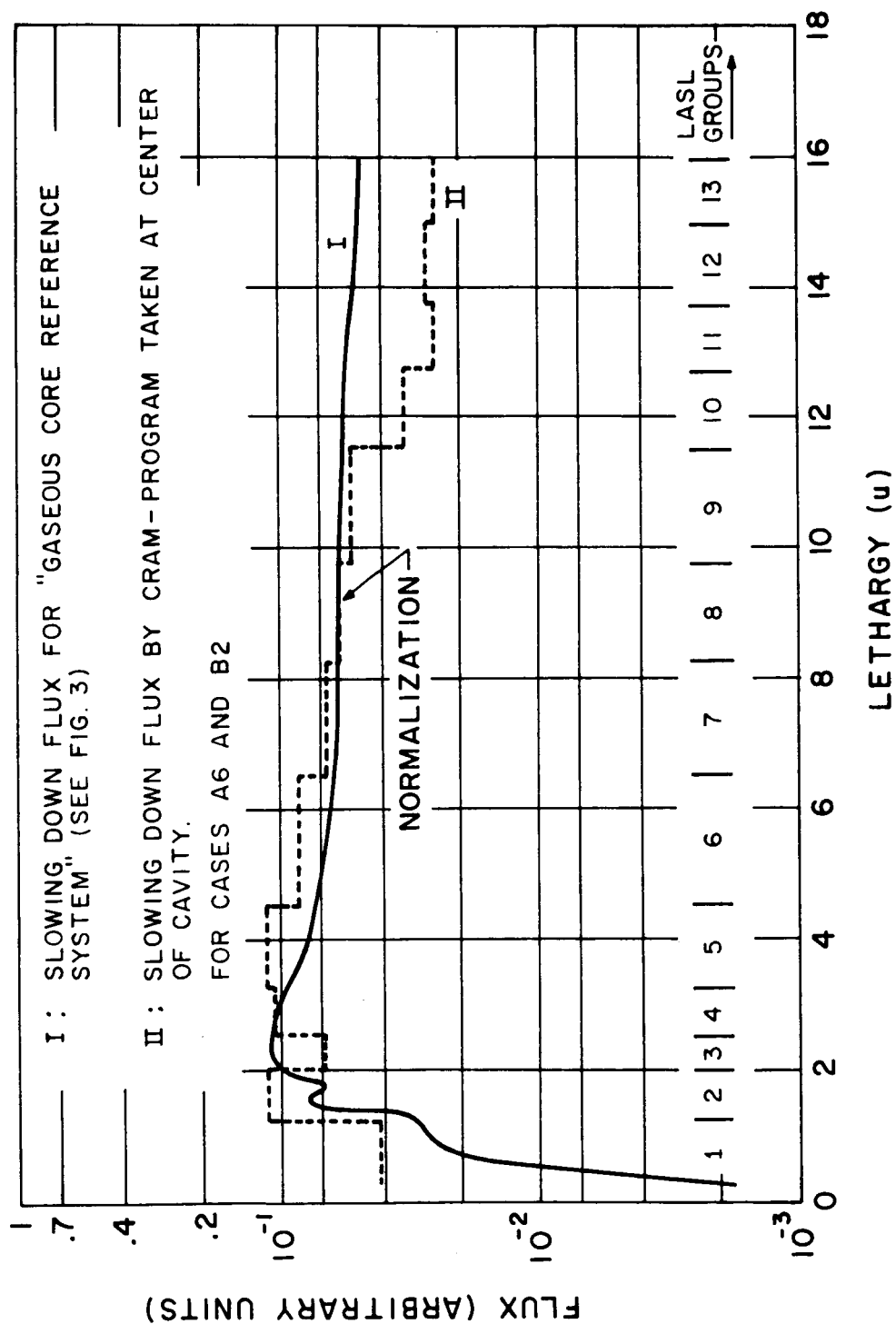


FIG. 9 COMPARISON OF SLOWING DOWN FLUXES



CRAM-program for cases A6 and B2\*. The second curve deviates considerably from the first. It shows a higher fast flux and a smaller thermal flux indicating a higher thermal leakage for the actual cases A6 and B2.

A first estimate of the effect of the deviation on the resonance cross sections can be made by consulting Fig. 4 and Table 9. If one extrapolates the curves in Fig. 4 to a buckling of approximately  $B = 0.09$  then the shape of the slowing down flux in Fig. 4 would correspond approximately to the shape of the slowing down flux for cases A6 and B2 in Fig. 9.

In Sec. 4.3, I examined the effect of the buckling on the resonance cross sections which is summarized in Table 9. Now extrapolating the bucklings in Table 9 to  $B \approx 0.09$  this would give a variation in cross section of approximately 1 per cent at most in comparison with a buckling  $B = 0.02245$ .

Therefore it can be concluded that, despite the relatively large differences in the slowing down fluxes, the effect of using the idealized slowing down flux as weighting spectrum instead of the actual one can be neglected.

Thus both the first part of the homogenization assumption concerning the spatial dependence and the second part concerning the energy dependence of the slowing down flux are verified.

## 5.2. Doppler Temperature Coefficient of Reactivity.

In Sec. 4.4 the Doppler coefficient of reactivity was determined using the resonance integrals calculated for a typical gaseous core reference system which corresponds approximately, with respect to the atomic densities, to the actual reactor system B2 of Sec. 5.1.1.

---

\* The relative difference between the two cases in a particular group is rather small (see previous section).

In this section the Doppler coefficient as determined in 4.4 and the Doppler coefficient for the actual reactor system B2 shall be compared. Because the latter was calculated using the CRAM program which in turn computes only the total reactivity coefficient and not specifically the Doppler coefficient, a process of elimination has to be used.

A basis for the following is that in the determination of the reactivity coefficient using the CRAM program only the resonance cross sections were changed (i.e., corresponding to temperatures of 300°k, 2320°k, and 40.000°k). Fast and thermal cross sections remained unchanged.

For a simplified system (bare homogeneous reactors with  $\epsilon = 1$ ) the temperature coefficient of reactivity splits up into the following parts:

a. Temperature variation of  $\eta = \nu/l + \alpha$  ( $\alpha$  = capture to fission ratio). Because of the low-lying fission and capture resonance in U-235  $\eta$  depends mainly on the neutron temperature which corresponds approximately to the moderator temperature. This temperature in turn, because of the large mean free path within the cavity, is equal to the reflector temperature which was assumed to be 300°k. Because the thermal cross sections in the calculations were left unchanged this suggests that the variation of the  $\eta$  with fuel temperature can be neglected.

b. Temperature variation of the thermal utilization  $f$ . Here the same arguments as in the previous point are valid, thus  $1/f \, df/dT$  can be neglected.

c. Temperature variation of  $\tau$ . Because the various moments of the slowing-down kernel involve only the scattering properties of the moderator this variation can be neglected.

d. Temperature variation of  $L^2$ . In a homogeneous reactor  $L^2$  is inversely proportional to the absorption and transport cross sections. According to Ref. 7 (p.488) this again depends on the properties of the moderator, i.e., its volume expansion coefficient and its temperature.

e. Temperature variation of the resonance escape probability  $p$ . This process of elimination shows that the CRAM program determines essentially the Doppler coefficient if only the resonance cross sections are varied because the variation of all the other factors (a to d) have no effect on the variation of the total reactivity coefficient.

A few remarks have to be made in connection with the above-mentioned points. Obviously the system investigated is not realistic. If the fuel temperature is changed from  $300^\circ\text{K}$  to say  $40.000^\circ\text{K}$  the surrounding reflector is heated up too, mainly by thermal radiation and fission fragments. Thus assuming a constant reflector temperature of  $300^\circ\text{K}$  makes the system quite unrealistic. The primary objective, however, is not the determination of actual temperature coefficients, but to prove that the reactivity changes calculated from the resonance integrals for the "idealized" homogeneous system correspond to the changes calculated for an actual system in which the fuel temperature is correspondingly varied.

A last remark concerns the thermal properties of the reactor. Points a to e are only valid for thermal reactors. Fortunately, a gaseous core reactor with its unconventional cavity properties is also a thermal reactor. This is due to the fact that for neutrons with energies higher than thermal the cavity is transparent, i.e., essentially no captures or fissions will occur in the cavity until the neutrons reach thermal energy.

The following reactivity changes were calculated:

$\Delta T [^{\circ}K]$	300 - 2320	2320 - 40.000
for gaseous core reference system (see 4.4)	-0.00104	-0.00006
k	1.000064	0.999504
for reactor system B2 (see 5.1.1)	0.999504	0.999444
$\Delta k$	-0.00056	-0.00006

The agreement at least in the higher temperature region is excellent. For the lower temperature region the agreement is not as good but still can be considered as reasonable because of the required high accuracy in the computation of these values. (The accuracy was increased up to the sixth significant figure.)

This again proves the assumption that a single gaseous core reference system can be used for the determination of the resonance cross sections instead of the actual ones.

### 5.3 Comparison With Measured Critical Masses

#### 5.3.1 For Spherical Systems

The first set of experimental data against which the calculated cross sections are checked were performed by D. V. P. Williams at ORNL (see Ref. 12) on Beryllium-reflected spherical reactors. The experiments used 10 mil Oy-foils and Be-blocks in a supporting Al-lattice. The relevant data are summarized in Table 11.

- The following table compares the critical masses which are
- Measured
  - Computed by C. B. Mills<sup>12</sup> using the LASL-16 group cross sections and the SNG-program<sup>15</sup>
  - Computed by author using

- α. the LASL-16 group cross section
- β. the revised LASL-16 group cross sections  
(designated by HRG)

source	experiment	Mills <sup>12</sup>	author	
			LASL**	HRG
sphere 1*	15.	10.	10.9	13.7
sphere 2*	7.7	7.3	7.15	8.36
sphere 3*	19.3	16.5	15.1	18.

Two major points with respect to these data are of importance:

- a. The comparison of results obtained by a transport program (SNG by Mills<sup>12</sup>) and a diffusion program (CRAM-16 group), and
- b. the comparison of calculated and measured critical masses.

As pointed out in Ref. 1 the relative difference in determined critical masses and slowing down fluxes between calculations using a transport program and calculations using a multigroup diffusion program are surprisingly small. It is shown that this is not only valid for homogeneous gaseous core reactors but also for reactors with extremely compressed fuel regions. This result suggests that the angular distribution of neutrons entering the core does not require a higher order representation than given by diffusion theory. In Sec. 5.4.1 it will be shown that this is only true if the region between compressed fuel and reflector is not a complete void.

The relative differences between the results obtained by

---

\* See Table 11.

\*\* Calculated for comparative purposes.

Mills and those obtained using the CRAM-program and the LASL-16 group cross sections lie between approximately 2-9 per cent. Although this cannot be considered a close agreement (as reported in Ref. 1) it still shows a high degree of equivalence between the two computational methods, especially when small differences in the basic data (e.g. percentage of admixtures) are taken into account. This confirms the assumption that a multigroup diffusion treatment is adequate for the calculation of gaseous core reactors.

A still more important result can be obtained by comparing the critical masses. The table shows that critical masses calculated with the revised resonance cross sections (HRG) are much closer to the measured ones than those obtained using the unrevised LASL-group cross sections. An exception is sphere 2. Here the measured critical mass is as close to the HRG-result as it is with respect to the LASL-result.

An even higher degree of agreement will be presented in the following section. One point in this connection needs to be mentioned. The experimental data for the above spherical systems were obtained not from the original paper but from Ref. 12. This usually introduces slight deviations in the basic data. Fortunately the data presented in the next section were taken from the original paper\*, thus, at least formally, a higher degree of accuracy can be expected.

### 5.3.2 For Cylindrical Systems

This set of experimental results obtained by G. A. Jarvis and C. C. Byers<sup>14</sup> is of particular interest because of two reasons. First, the experiments were performed using a cylindrical geometry, which is the geometry interesting from the engineering standpoint and secondly the experiments checked the influence of interior and exterior fuel compression.

---

\* Obtained by private communication from G. A. Jarvis.

Three experiments were performed:

In experiment 1 the fuel elements were approximately uniformly distributed throughout the cavity volume.

In experiment 2 the oralloy-loaded graphite fuel elements were concentrated towards the center of the cavity. The fuel-occupied zone was between  $r = 0$  and  $r = 16.65$  cm leaving a void column between fuel and reflector. In the next section this shall be abbreviated as "interior" fuel compression.

In experiment 3 the fuel elements were concentrated towards the wall of the cavity leaving an inner void column between  $r = 0$  and  $r = 10$  cm. This shall be abbreviated as "exterior" fuel compression.

In the recalculation of the experiments not the critical masses but the effective multiplication factors were determined in order to save computer time (for dimensions and configuration of the experimental cylinders see Table 12 and Fig. 10).

	experiment 1 (homog. filling)	experiment 2 (interior compr.)	experiment 3 (exterior compr.)
measured critical masses [kg U-235]	7.62	8.63	7.325
$k_{\text{eff}}$ by Mills <sup>12*</sup>	1.02	0.93	—
$k_{\text{eff}}$ by author**	1.026	1.0065	1.0019

---

\* C. B. Mills used the SNG-program<sup>15</sup> and the LASL-16 group cross sections. Furthermore, the reactors were calculated as "equal cavity volume spheres," i.e., the cavity radii were scaled at: cylindrical volume for experiments = spherical volume for recalculation.

\*\* Using the CRAM-program with the revised LASL-16 group cross sections. For the resonance cross section the  $0.5 \times 10^4$ - set for  $T = 300^\circ\text{K}$  was used (see Table 7). In experiments 2 and 3 (void cases) the void region was filled with  $5.0 \times 10^{17}$  Be-atoms/cm<sup>3</sup> in order to have a non-zero diffusion coefficient in this region. Its influence on the results is negligible. The mesh-width (checked for space-differencing errors) for the calculations are summarized in the following table.

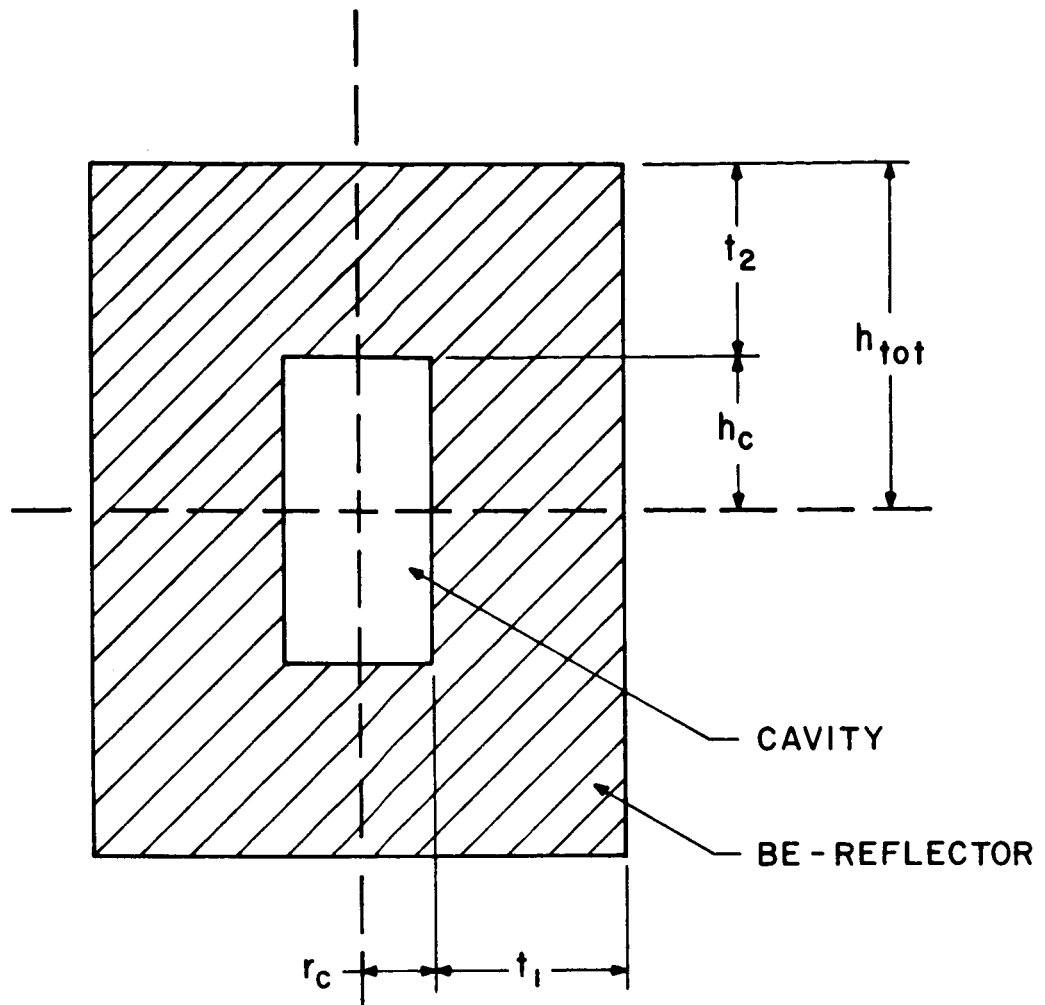


FIG. 10 CONFIGURATION OF CYLINDRICAL EXPERIMENTAL REACTORS .



### R-direction

experiment	inner void column	mesh width in fuel region	outer void column	mesh width in reflector
1,2,3	0(3.333 cm)3	3(2.2167 cm)6	6(1.5018 cm)8	8(7.832 cm)14

### Z-direction

experiment	mesh width in cavity	mesh width in reflector
1,2,3	0(5.5617 cm)6(3.0 cm)8	8(7.622 cm)14

One check-run was performed to determine the critical mass for experiment 1. The calculated critical mass was 0.6 per cent smaller than the measured one. This run took 2 hr. 6 min. on an IBM 7094 computer.

As the table shows the computed reactivity coefficients using the CRAM-program for two-dimensional geometry are in good agreement with the experimental results for experiments 2 and 3, i.e. for interior and exterior fuel compression. The recalculated experiment 1 shows a 3 per cent-deviation from the required value unity. A possible explanation for the latter deviation is the following: In experiments 2 and 3 the fuel rods in the fuel region were closely spaced whereas in experiment 1 the gaps between the fuel rods were much larger because the rods were distributed over the whole cavity. In the recalculation of the experiments the fuel region was assumed to be homogeneously filled with the fuel material corresponding to the required critical mass. Thus a possible explanation of the deviation of experiment 1 is that in this experiment the widely spaced fuel rods cannot be as well represented by a homogeneous filling as the more closely spaced fuel rods in experiments 2 and 3.

Still the evidence given by experiments 2 and 3 is good enough to conclude that the use of the computed resonance cross sections gives good agreement with experimental results. Because of the large computer time involved no attempt was made to do the same calculations with the "pure" LASL-16 group cross sections.

The "good agreement" stated above has to be understood as a value given to the relative theoretical error of the computations. Even in more sophisticated calculations the result is considered as reasonably good if the theoretically calculated effective multiplication factor lies within  $\pm 1$  per cent of the measured one.

However, I should like to point out that quite a different accuracy requirement has to be attached to the absolute error allowable in the computations. One way to achieve an at least qualitative basis is to compare a conventional (i.e., earthbound) reactor with a gaseous core reactor used as a rocket propulsion device for say interplanetary travel. Assuming that the fuel loading for these two reactors corresponds to a multiplication factor somewhat less than the required value, then the lifetime energy output of both reactors is less than the predicted one. For the conventional reactor this would mean that the power cycle is shorter than expected. Although this is not desirable it is not as crucial as for the gaseous core propulsion device. In the latter fuel and propellant supply, payload, transfer orbit etc., have been accurately determined for the expected power period. Thus a shorter power cycle would endanger or even lead to a failure of the mission. It can be concluded that gaseous core reactors intended for rocket propulsion devices require extremely accurate criticality calculations.

No comparison with Mills results shall be made because there a volume analogy was used\* and the error introduced by such a method cannot be determined exactly because it depends on the specific cases.

A last point concerns the behavior of the critical mass under interior and exterior fuel compression. As the experiments show the critical mass is seen to increase if the fuel is compressed towards the axis of the cylinder and decreases if the fuel is compressed towards the wall of cavity. As it will be shown in the following section the latter depends on the geometry, i.e. the ratio of the inner fuel radius to total cavity radius, and is furthermore affected by the presence of scattering material (e.g., hydrogen) in the cavity.

#### 5.4 Variations of Critical Mass Under "Interior" and "Exterior" Fuel Compression

Although the results presented in this section essentially do not fall within the scope of this report they shall be briefly discussed in order to point out some of the engineering aspects of gaseous core reactors one of which is the question of critical mass behavior when the gaseous fuel is compressed. Furthermore, the effect of hydrogen within the cavity is considered.

In order to simplify the presentation of the various parameters which occur when fuel is compressed two general compression parameters are defined:

Exterior compression parameter  $P_{\text{ext}} = a/r_c$

Interior compression parameter  $P_{\text{int}} = b/r_c$

---

\* A similar method, the "buckling analogy" was applied in Ref. 16 in order to save computer time. There the bucklings (including the unknown reflector savings) for sphere and cylinder were equated.

a = distance of fuel region from axis  
b = distance of fuel region from cavity surface  
 $r_c$  = cavity radius

Figure 11 shows the basic compression cases and the corresponding values for the compression parameters.

All the following results have been obtained for the following set of data:

1. Spherical geometry  
cavity radius = 80 cm; reflector thickness = 100 cm
2. Reflector = graphite with  $n_c = 8.38 \times 10^{22}$  at/cm<sup>3</sup>
3. HRG-resonance cross sections
4. Over-all reactor temperature: 300°k

#### 5.4.1 Fuel Compression Without Hydrogen

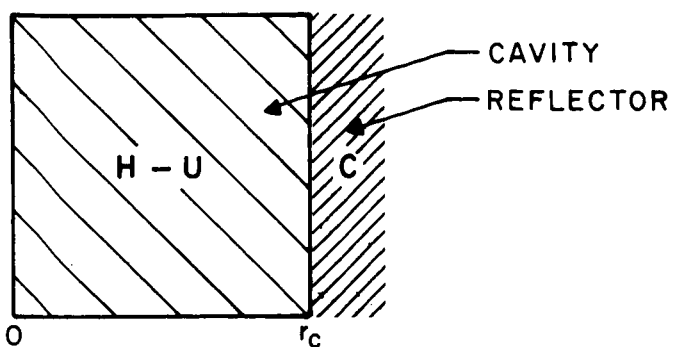
In this section the region between fuel and reflector (in case of interior compression) and between fuel and axis (in case of exterior compression) is treated as a void. In order to have a non-zero diffusion coefficient, a finite but extremely low hydrogen density was introduced in the void region. Its effect on the computed critical masses is negligible.\* In case of interior compression the void region was treated as one radial mesh. This last assumption needs some clarification\*\*. If the void region is treated as one mesh it is assumed that all neutrons leaving the reflector will penetrate the fuel region. However, if the fuel is compressed toward the axis the probability for the neutrons of "finding" the fuel region decreases. Thus, by neglecting this pure geometrical effect the critical mass will be underestimated.

---

\* A check run showed that an increase of the hydrogen density by one order of magnitude resulted in a critical mass change in the fourth significant figure.

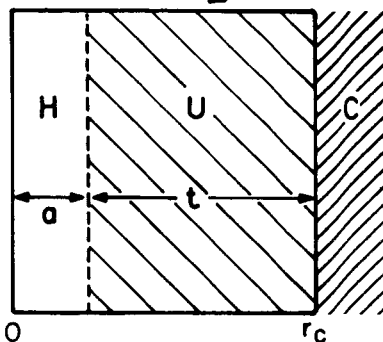
\*\* A more detailed discussion is left to a later report.

# HOMOGENEOUS CASE

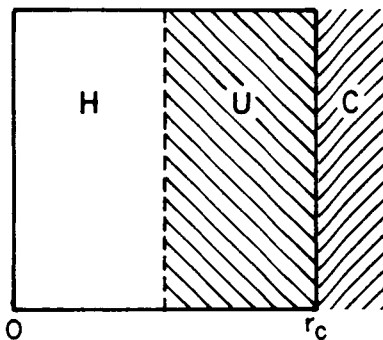


## EXTERIOR COMPRESSION

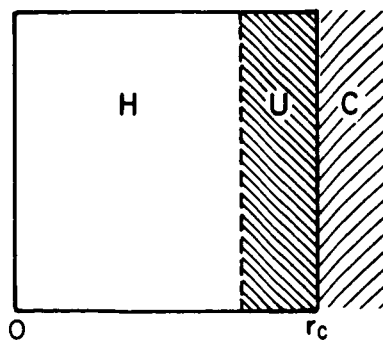
$$P_{\text{ext}} = \frac{a}{r_c}$$



$$a = \frac{1}{4} r_c \rightarrow P_{\text{ext}} = \frac{1}{4}; (t = \frac{3}{4} r_c)$$



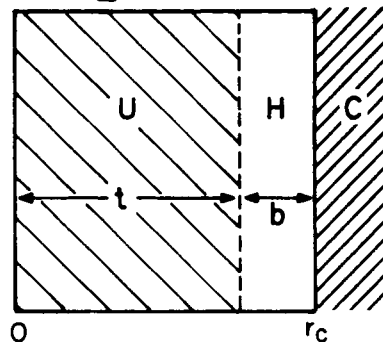
$$a = \frac{1}{2} r_c \rightarrow P_{\text{ext}} = \frac{1}{2}; (t = \frac{1}{2} r_c)$$



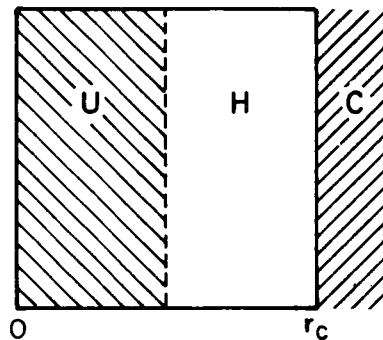
$$a = \frac{3}{4} r_c \rightarrow P_{\text{int}} = \frac{3}{4}; (t = \frac{1}{4} r_c)$$

## INTERIOR COMPRESSION

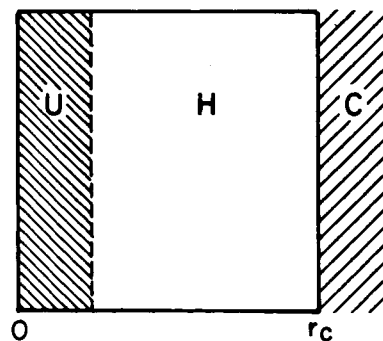
$$P_{\text{int}} = \frac{b}{r_c}$$



$$b = \frac{1}{4} r_c \rightarrow P_{\text{int}} = \frac{1}{4}; (t = \frac{3}{4} r_c)$$



$$b = \frac{1}{2} r_c \rightarrow P_{\text{int}} = \frac{1}{2}; (t = \frac{1}{2} r_c)$$



$$b = \frac{3}{4} r_c \rightarrow P_{\text{ext}} = \frac{3}{4}; (t = \frac{1}{4} r_c)$$

FIG. II BASIC COMPRESSION CASES

The opposite is true if the void region is divided into a large number of mesh regions. Butler and Chang<sup>18</sup> showed that thermal neutrons leaving the reflector and entering the void region have angular distributions strongly peaked toward the axis. Because the diffusion approach applied in the present calculations does not take into account angular effects, the treatment of the void (divided into a large number of mesh regions) by diffusion theory, which assumes isotropic scattering in the laboratory system, results in an overestimate of the critical mass.

In this connection the method applied for the computation of critical masses under interior fuel compression in the following Sec. 5.4.2 shall be mentioned. In Sec. 5.4.2 the void region is filled with hydrogen having approximately twice the atomic density than the fuel in the fuel region. Computations show that in this case the treatments of the void region as one mesh or as a large number of mesh regions result in the same critical mass. This is due to the fact that hydrogen now acts as an added reflector. Thus, by definition, the geometrical probability for neutrons (leaving this added reflector region) of entering the adjacent fuel region is unity.

For the case of exterior fuel compression the computations showed no difference in critical mass if the interior void region was treated as one or more mesh regions for both low and high hydrogen densities in this region.

The following table lists the critical data obtained for the compression cases without hydrogen:

TABLE C

Case	Type of compression	Compression parameter	$n_H$ [at/cm <sup>3</sup> ]	$n_U$ [at/cm <sup>3</sup> ]	$\frac{n_H}{n_U}$	$m_{cr}$ [kg]
C1*	Homog.	—————	0	$1.1293 \times 10^{19}$	0	9.45
C2	—————	$p_{ext} = 1/4$	$1.0 \times 10^{17}$	$1.2403 \times 10^{19}$	0.008	10.22
C3	Exterior	$p_{ext} = 1/2$	$1.0 \times 10^{17}$	$1.308 \times 10^{19}$	0.008	9.57
C4		$p_{ext} = 3/4$	$1.0 \times 10^{17}$	$1.455 \times 10^{19}$	0.007	7.04
C5	Interior	$p_{int} = 1/4$	$2.0 \times 10^{17}$	$3.1465 \times 10^{19}$	0.006	11.11
C6	Interior	$p_{int} = 1/2$	$2.0 \times 10^{17}$	$3.278 \times 10^{19}$	0.006	34.29
C6'	***Interior	$p_{int} = 1/2$	$2.0 \times 10^{17}$	$2.765 \times 10^{19}$	0.007	28.9

\* For comparison.

\*\* Equal case C6 except for the use of the unrevised LASL-16 group cross section set.

The critical masses of the above table are plotted versus the compression parameters  $p_{ext}$  and  $p_{int}$  in Fig. 12. If the fuel is compressed towards the interior, the critical mass is seen to increase continuously up to  $p_{int} = 1/2$ . As shown in the next Sec. 5.4.2 it will then decrease for  $p_{int} \gtrsim 5/8$ . For exterior compression the critical mass first rises above the value for a homogeneous filling and then decreases for  $p_{ext} > 1/4$ . It has approximately the same value for  $p_{ext} = 1/2$ . The cylindrical experiments cited in the preceding section showed for experiment 3, having a  $p_{ext}$  of approximately  $1/2$ , a decrease of critical mass from the homogeneous case (experiment 1). Because the data presented here were calculated for a spherical system this indicates that the geometry has an effect on the compression behavior.

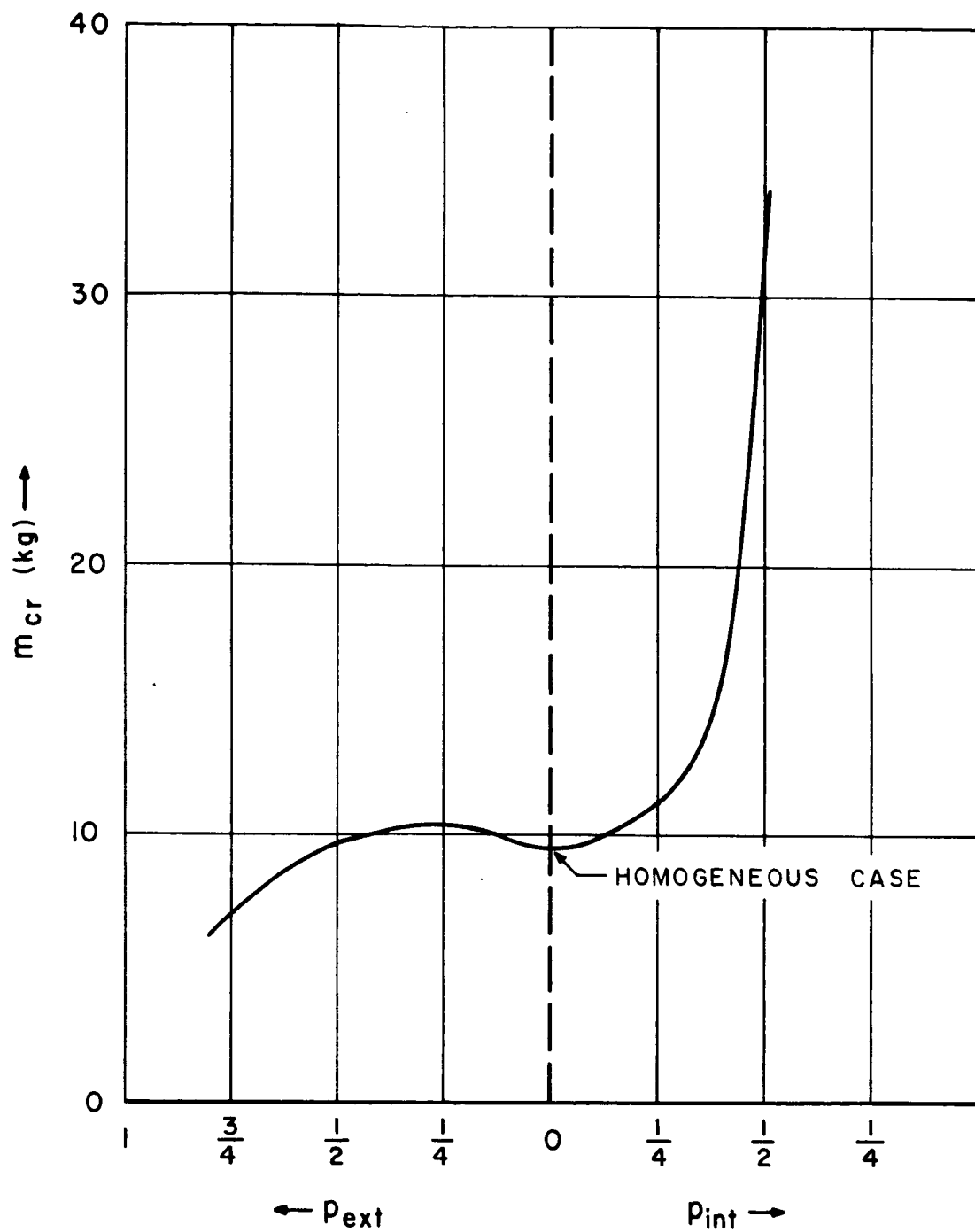


FIG. 12 INTERIOR AND EXTERIOR FUEL COMPRESSION  
WITHOUT HYDROGEN



An explanation for the curve in Fig. 12 can be given by observing the behavior of the thermal flux in the fuel region. Figure 13 shows a plot of the thermal flux versus cavity radius for the three cases C1, C3, and C5.

That the explanation has to be found in the behavior of the thermal flux and not in fluxes corresponding to higher energy groups is evident from Table 10A. Here the fluxes (in arbitrary units) are listed as a function of radius for the 4 lowest energy groups. The case with highest thermal flux depression, i.e. the interior compression case C5, is taken as an example. It can be observed that most of the spatial self shielding occurs in the "thermal" groups and is decreasing with higher neutron energy. In the first epithermal group (group 13: 1-3eV) the flux depression is small compared to the three lower (in energy) groups.

Thus an increase or decrease of the critical mass has to be determined by the thermal utilization indicated by a lower or higher thermal flux respectively.

Going back to the flux plots in Fig. 13 one observes the following points:

1. The average thermal flux in the fuel region for interior fuel compression (case C5) is smaller than the average thermal flux for the homogeneous case.
2. The same is true for exterior compression (case C3) although the relative difference is considerably smaller.

Physically the above trends of the thermal flux can be explained by the following:

1. The strong depression of the thermal flux for interior compression is simply due to the spatial self-shielding as the result of the decreasing fuel radius and thus the increasing fuel density.

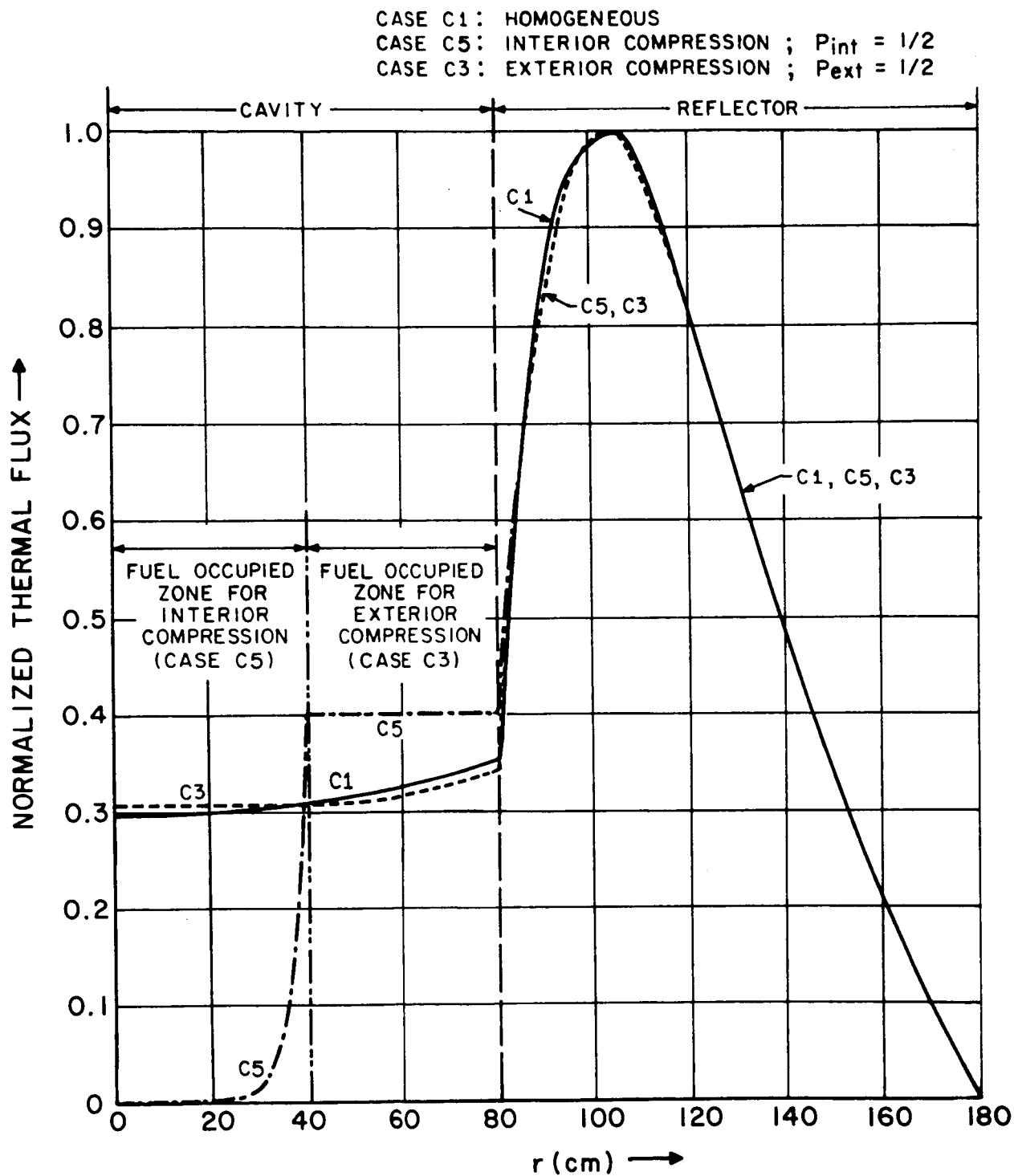


FIG. 13 THERMAL FLUXES FOR COMPRESSION CASES  
(WITHOUT HYDROGEN)

2. The behavior for exterior compression is less well explainable because a negative and a positive effect are superimposed upon each other. If fuel is re-moved from the central region the fast flux decreases and the thermal flux increases in this region (see Ref. 17). Also the adjacent fuel region has a higher thermal flux as compared to the thermal flux before the central fuel was removed. Because the fuel in the exterior compression case is not removed but compressed toward the wall of the cavity an additional spatial self-shielding occurs.

This spatial self-shielding depends on the geometry considered. If a cylindrical and a spherical cavity, having equal volume and the same exterior compression parameter  $p_{ext}$ , are compared the compression in the cylinder is stronger and therefore the spatial self-shielding is higher than in the sphere. However, in a cylindrical cavity the fuel and the hydrogen region extend from top to bottom and the thermal flux near the top and bottom reflector is increased (see Ref. 2). This diminishes the stronger spatial self-shielding. As to what extent the stronger spatial self-shielding is overcome depends on geometrical factors like length-to-diameter ratio, exterior compression parameter, etc. This is the geometrical effect mentioned above resulting in a different compression behavior for the cylindrical experiments and the spherical calculations.

Thus the thermal flux in the compressed fuel region increases due to the "removal" and decreases due to the spatial self-shielding. No definite conclusion seems possible. However, the calculations indicate that in spherical cavities the "removal" effect is greater than the spatial self-shielding effect only for  $p_{ext}$  slightly greater than  $1/2$ .

#### 5.4.2 Fuel Compression With Hydrogen.

As mentioned several times in this report the presence of hydrogen within the cavity has a strong influence on the critical mass. In this section some of the effects shall be considered. In order to reduce the parameters involved certain restriction are made which reduce the parameters to those occurring in the actually considered gaseous core reactor devices.

1. The cases with interior fuel compression are representative for the so-called "coaxial flow devices" in which fuel and the surrounding hydrogen form two coaxial streams, injected at the top of the cylindrical cavity and exhausted through a nozzle at the bottom. Hydrogen is heated mainly by thermal radiation. A first estimate is that the fuel temperature is approximately twice the hydrogen temperature. Thus, in equilibrium the ratio of the atomic densities in the two regions is given by:

$$\frac{\text{atomic density in outer region}}{\text{atomic density in inner region}} = \frac{n_H}{n_U} = \frac{T_F}{T_H} = 2$$

$T_F$  = fuel temperature

$T_H$  = hydrogen temperature.

The following table lists the interior compression cases for  $n_H/n_U \approx 2$ .

$P_{int}$	$n_H$ [at/cm <sup>3</sup> ]	$n_U$ [at/cm <sup>3</sup> ]	$n_H/n_U^*$	$m_{cr}$ [kg]
homog.**	$2.302 \times 10^{19}$	$1.124 \times 10^{19}$	2.05	9.4
1/4	$5.977 \times 10^{19}$	$2.992 \times 10^{19}$	2.0	10.56
1/2	$3.920 \times 10^{19}$	$1.804 \times 10^{20}$	2.17	18.87
5/8	$3.082 \times 10^{22}$	$1.409 \times 10^{22}$	2.19	621.6
3/4	$4.436 \times 10^{22}$	$2.181 \times 10^{22}$	2.03	285.1
9/10	$9.465 \times 10^{22}$	$5.715 \times 10^{22}$	1.66	47.9

\* The error introduced by the deviation from  $n_H/n_U = 2$  is approximately  $\pm 2$  per cent.

\*\* For comparison.

Figure 14 gives a plot of the required critical masses versus the interior compression parameter  $p_{int}$ . With increasing  $p_{int}$  the critical mass is seen to increase until it reaches a maximum at  $p_{int} = 5/8$ . With further increasing  $p_{int}$  the critical mass decreases. The point for  $p_{int} = 9/10$  is only of theoretical interest because the required critical uranium density is higher than for solid Uranium 235.

This behavior can be explained by consulting Fig's. 15A, 15B, and 15C in which fast and thermal fluxes (in arbitrary units but in all three figures to the same scale) are plotted versus the cavity radius for  $p_{int} = 1/2$ ,  $5/8$ , and  $9/10$  respectively. Figure 15A shows a fast flux extremely low in comparison with the thermal flux. The spatial self-shielding in the fuel region is not as strong as in the case without hydrogen (see case C5 in Fig. 13). This is due to the added slowing down region between fuel and reflector.

Figures 15B and 15C show a rather high fast flux in the fuel region and an extremely strong spatial self-shielding in the fuel region. Obviously the assumption made previously to neglect the surface term in the calculation of the resonance integrals breaks down completely for these extreme compressions. Fortunately they are only of theoretical interest because of the extremely high pressures required to confine the fuel.

A possible explanation for the steep increase of  $m_{cr}$  between  $p_{int} = 1/2$  and  $p_{int} = 5/8$  and the steep decrease between  $p_{int} = 5/8$  and  $p_{int} = 9/10$  is that for the former the hydrogen density is not high enough to overcome the spatial self-shielding whereas for the latter the hydrogen density is so high that it acts as the sole reflector (no neutron reaches the graphite reflector) thus increasing the thermal flux at the edge of the fuel region extremely. In addition a comparison

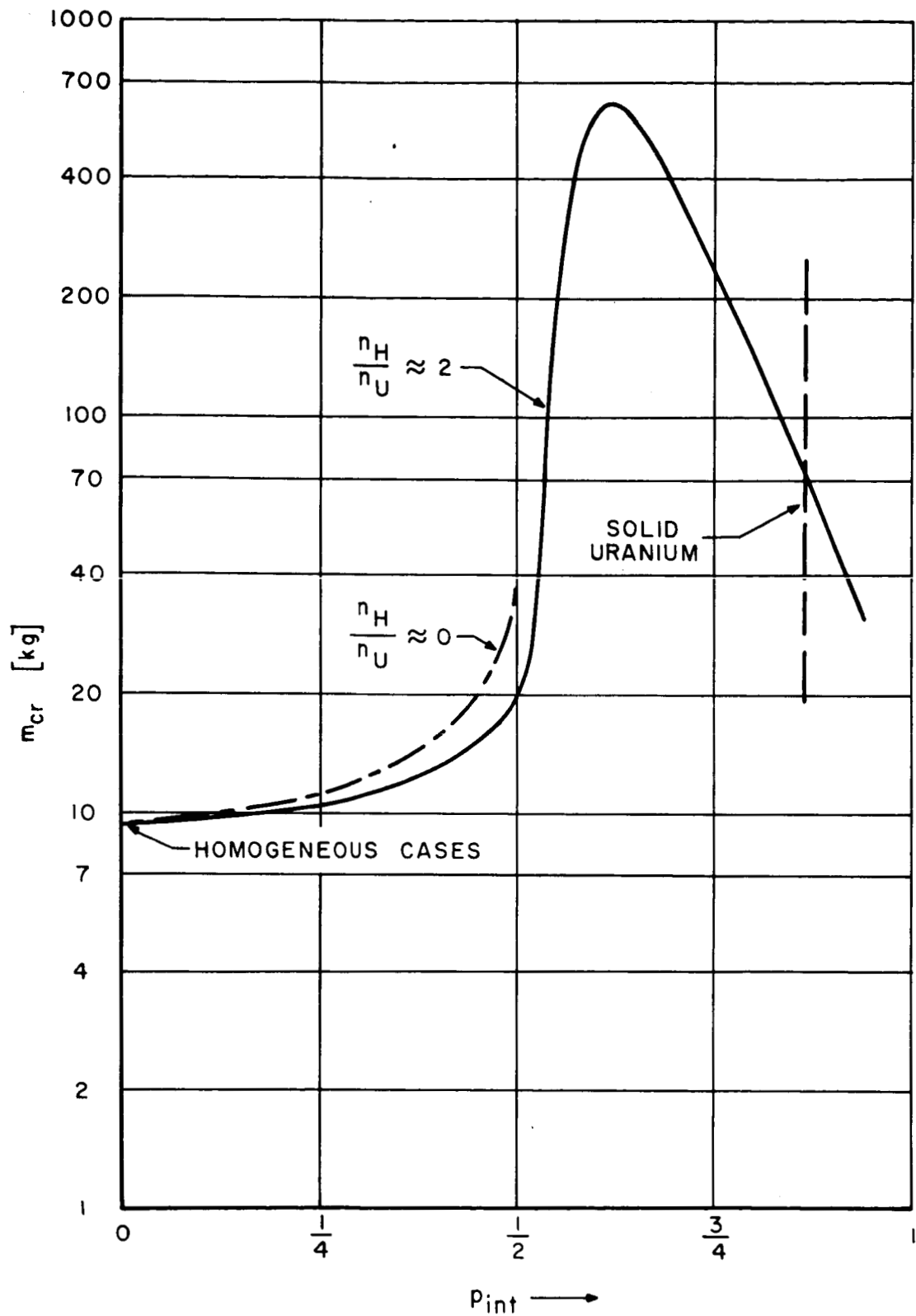


FIG. 14 INTERIOR FUEL COMPRESSION WITH HYDROGEN

$$\frac{n_H}{n_U} = \frac{\text{HYDROGEN ATOMIC DENSITY IN OUTSIDE REGION}}{\text{URANIUM ATOMIC DENSITY IN FUEL REGION}}$$

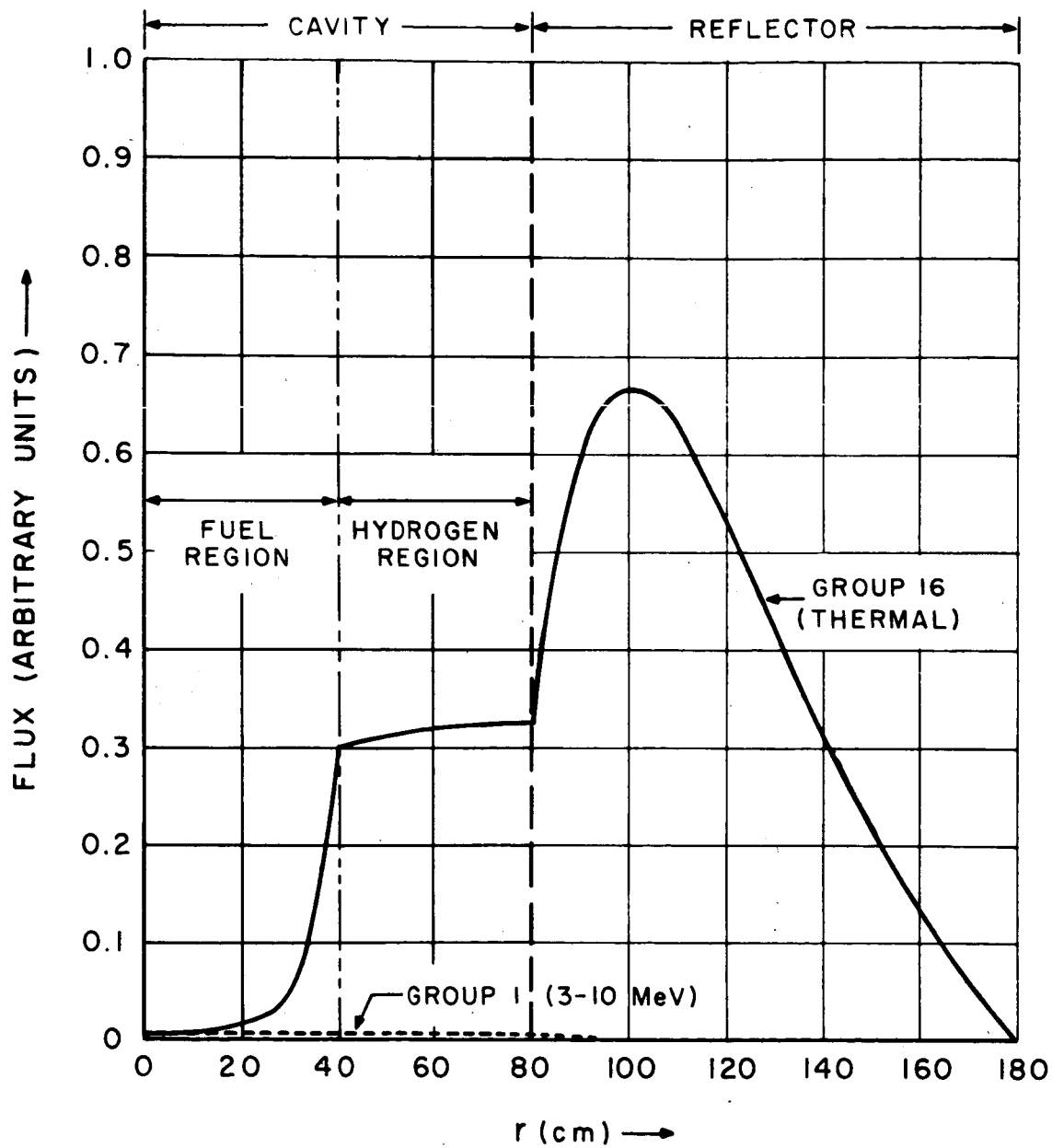


FIG. 15A FAST AND THERMAL FLUX FOR  $P_{int} = 1/2$   
(WITH HYDROGEN)

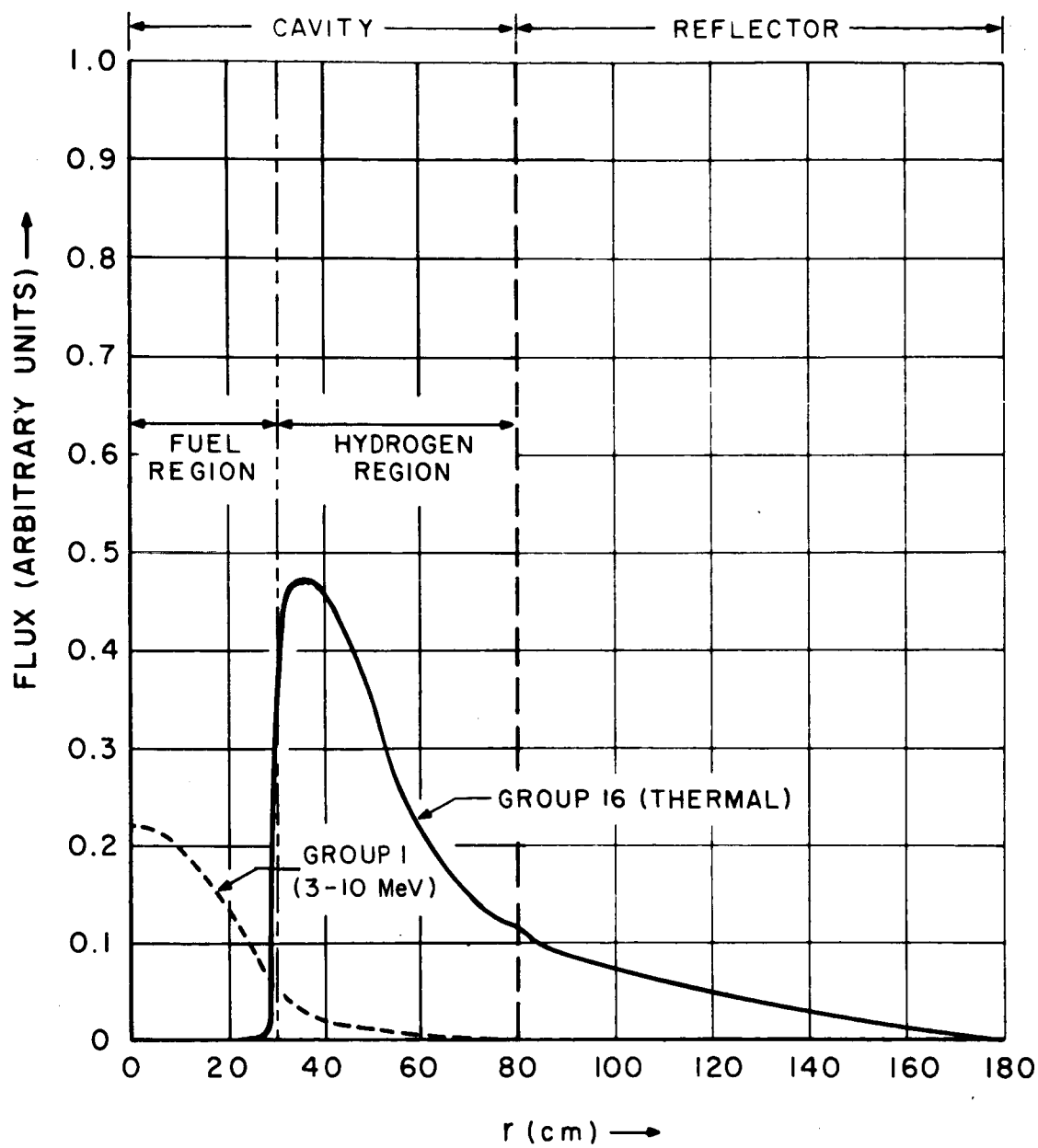


FIG. 15B FAST AND THERMAL FLUX FOR  $p_{int} = 5/8$   
( WITH HYDROGEN )



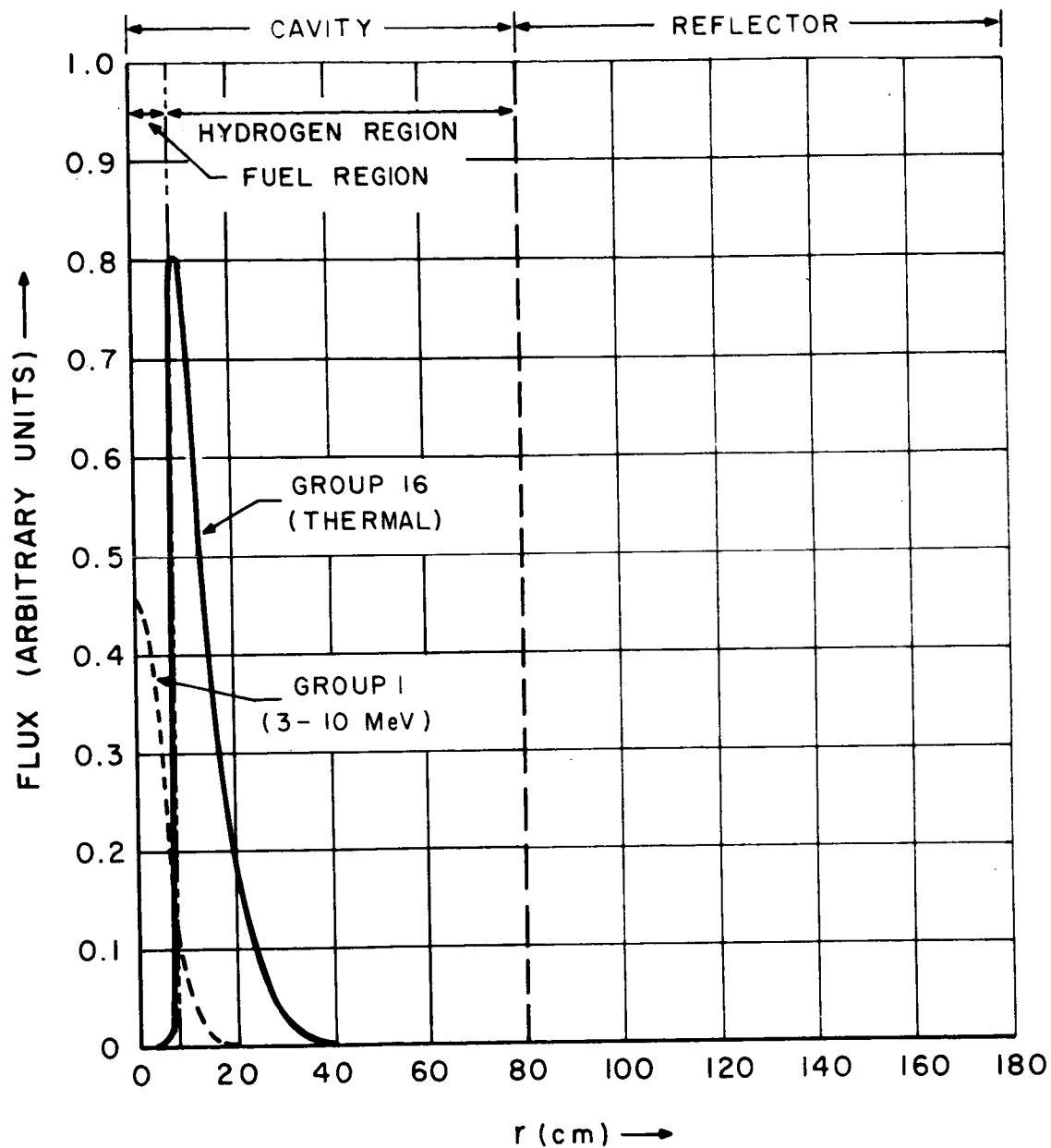


FIG. 15C FAST AND THERMAL FLUX FOR  $P_{int} = 9/10$   
(WITH HYDROGEN)

of the fast fluxes shows that more fast fissions will occur for  $p_{\text{int}} = 9/10$  as compared to  $p_{\text{int}} = 5/8$ .

2. The cases with exterior fuel compression resemble approximately the so-called "vortex flow devices" in which both fuel and hydrogen are introduced at the cylindrical cavity walls and are rotated by mechanical or electrical means. Due to the centrifugal forces fuel is compressed toward the cavity walls and hydrogen which diffuses through the fuel region forms the inner column. Heat is transferred mainly by molecular interaction. A first estimate is that both fuel-and-hydrogen temperatures are equal. Thus, the requirement for equilibrium is:

$$n_{\text{H}_{\text{int}}} = (n_{\text{H}} + n_{\text{U}})_{\text{ext}}$$

$$n_{\text{H}_{\text{int}}} = \text{hydrogen density in inner region}$$

$$n_{\text{H}_{\text{ext}}} = \text{hydrogen density in outer region (accounting for the hydrogen diffusing through the fuel region)}$$

$$n_{\text{U}_{\text{ext}}} = \text{fuel density in outer region.}$$

The following parameter, which is also an important parameter occurring in the fluid dynamics calculations of this device, has been chosen:

$$\left\langle \frac{n_{\text{H}}}{n_{\text{U}}} \right\rangle_{\text{ext}} = \text{average hydrogen-to-uranium density ratio in the outer region.}$$

The following critical masses were calculated:

$\left\langle \frac{n_{\text{H}}}{n_{\text{U}}} \right\rangle_{\text{ext}}$	$p_{\text{ext}}$		
	1/4	1/2	3/4
0.01	9.45	9.48	9.29
10.	8.88	8.41	7.90
70.	6.2	6.0	5.42

In Figure 16 the critical masses are plotted against the exterior compression parameter  $p_{\text{ext}}$ . They are extrapolated at the right to the homogeneous cases with corresponding  $n_{\text{H}}/n_{\text{U}}$ -ratios. The critical mass is seen to decrease with increasing  $n_{\text{H}}/n_{\text{U ext}}$  for constant  $p_{\text{ext}}$ . Figure 17 gives a plot of the normalized thermal flux versus the radius for  $n_{\text{H}}/n_{\text{U ext}} = 0.01$  and 70. The thermal flux in the fuel region increases with higher hydrogen content thus increasing the thermal utilization and decreasing the critical mass.

It is also evident from Fig. 16 that the presence of hydrogen modifies the compression behavior considerably. For  $n_{\text{H}}/n_{\text{U ext}} = 10$  the critical mass still increases from the homogeneous case up to  $p_{\text{ext}} = 1/4$  and then decreases, whereas for  $n_{\text{H}}/n_{\text{U ext}} = 70$  the critical mass decreases continuously.

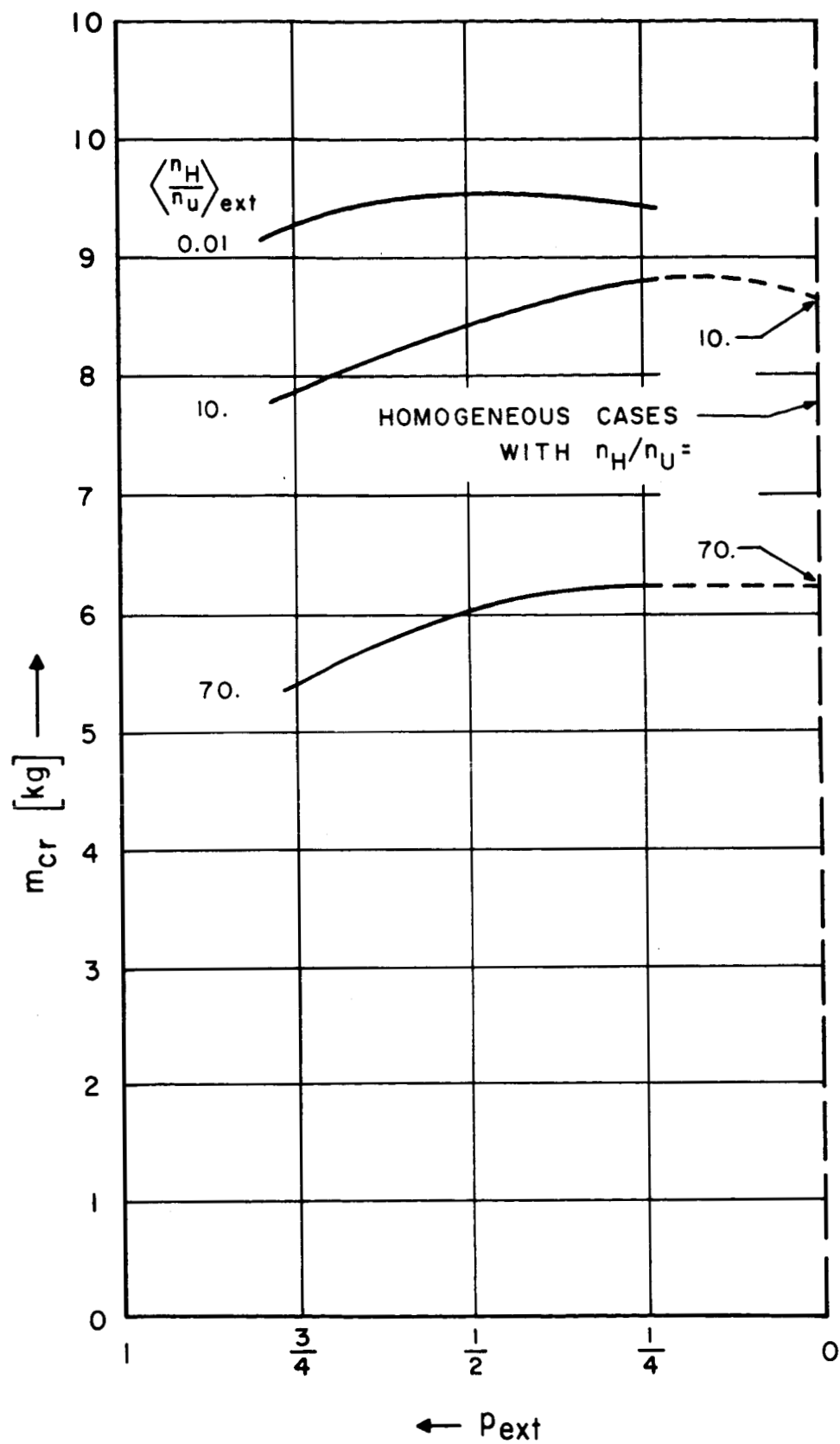


FIG. 16 EXTERIOR FUEL COMPRESSION WITH HYDROGEN

$$\left\langle \frac{n_H}{n_U} \right\rangle_{ext} = \frac{\text{HYDROGEN ATOMIC DENSITY IN FUEL REGION}}{\text{URANIUM ATOMIC DENSITY IN FUEL REGION}}$$

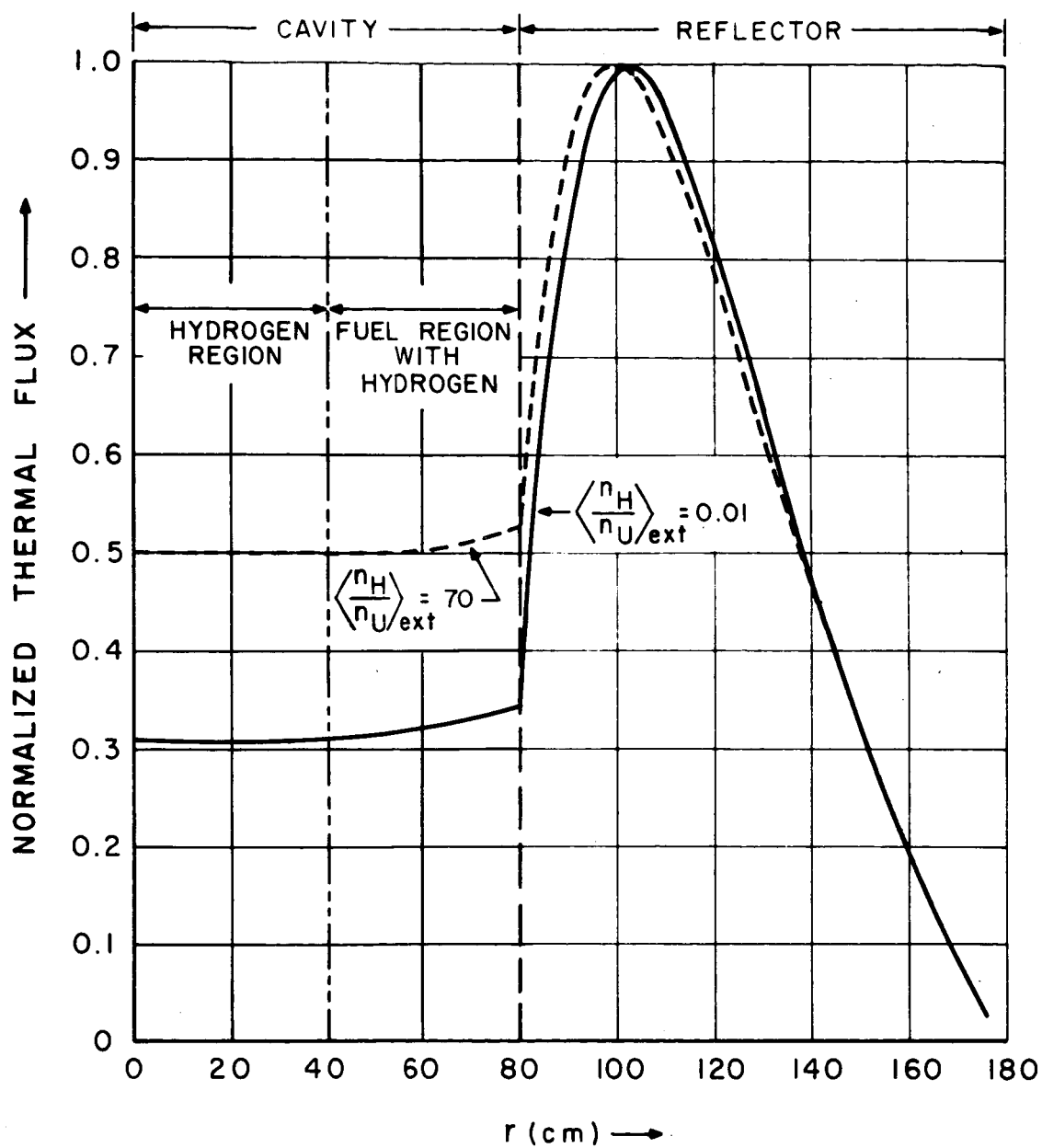


FIG. 17 THERMAL FLUXES FOR EXTERIOR COMPRESSION  
( WITH HYDROGEN )

## 6. CONCLUSION

The new set of resonance cross sections determined for an almost completely thermal U-235 gaseous core reactor system compares successfully with measured results both with respect to the effective resonance integrals and also when applied to recalculate measured critical masses. The Doppler temperature coefficients resulting from these new resonance data are shown to be of significant importance in the low temperature range between 300 and 2320°K and have to be taken into account for more accurate critical mass calculations. The homogenization assumption applied in the computation of the resonance data is verified both with respect to its effect on the spatial and energy dependence of the slowing down flux. It breaks down only for cases with extreme interior compression which are, however, not of practical interest because of the extreme cavity pressures required.

Some of the phenomena interesting in connection with the considered actual gaseous core reactors are evaluated. Of particular interest is the influence of hydrogen on the critical masses. Further research is intended along this line including thermalization problems and optimization calculations.

TABLE 1

DOPPLER WIDTHS AT VARIOUS TEMPERATURES AND  
RESONANCE ENERGIES [ev]

$E_i$ Temp.	1ev	20ev	1kev
300°K	0.0208	0.0928	0.656
2320°K	0.0583	0.261	1.842
5800°K	0.0923	0.412	2.92
10000°K	0.121	0.54	3.82
40000°K	0.242	1.08	7.65

TABLE 2

SOME RESONANCE DATA

Uranium 235:

resolved resonances:  $1.14 \text{ ev} \div 19.30 \text{ ev}$   
(all calculated with IM-approximation, except 10.6 ev resonance)  
average spacing 0.7 ev

unresolved resonances:  $20 \text{ ev} \div 3 \text{ Kev}$   
mean level spacing = 0.6561 ev  
 $\Gamma_n^0 = 1.32 \times 10^{-4} \text{ ev}$   
 $\Gamma_\gamma = 2.577 \times 10^{-2} \text{ ev}$   
 $\Gamma_f = 5.15 \times 10^{-2} \text{ ev}$   
statistical weight = 0.5

Uranium 238:

resolved resonances:  $6.68 \div 997 \text{ ev}$

unresolved resonances:  $1 \text{ Kev} \div 2.5 \text{ Kev}$   
mean level spacing = 20.6 ev  
 $\Gamma_n^0 = 2.03 \times 10^{-3} \text{ ev}$   
 $\Gamma_\gamma = 2.5\gamma \times 10^{-2} \text{ ev}$   
statistical weight = 1.0



TABLE 3

EFFECTIVE RESONANCE INTEGRALS FOR U-238

T[°K]	$\sigma_s^*$	RR = resolved resonances URR = unresolved resonances									
		12.75	72.75	102.7	302.8	10 <sup>3</sup>	3000	10 <sup>4</sup>	10 <sup>5</sup>	10 <sup>6</sup>	10 <sup>8</sup>
300	RR + URR	8.15	21.96	26.49	46.99	86.65	141.23	205.22	264.98	273.72	275.01
	RR			25.11				202.91			272.65
	URR			1.38				2.31			2.36
2320	RR + URR							236.30			
	RR										
5800	URR										
	RR + URR							246.49			
	RR										
10000	URR										
	RR + URR			46.56				249.51			273.98
	RR			45.57							272.65
40000	URR			0.99							1.33
	RR + URR							260.85			
	RR							260.23			
	URR							0.62			

(Values for T = 2320°K to 40,000°K inaccurate)

TABLE 4A

U-235 EFFECTIVE RESONANCE INTEGRALS FOR RESOLVED REGION

Temp.	Res. Integr.	$\sigma_s^*$	110.75	$10^3$	$10^4$	$10^8$
300	$I_{n,\gamma}$		29.33	55.13	68.16	70.55
	$I_f$		44.54	75.72	90.68	93.42
	$I_{abs}$		73.87	130.85	158.84	162.97
2320	$I_{n,\gamma}$				69.26	
	$I_f$				91.85	
	$I_{abs}$				161.11	
5800	$I_{n,\gamma}$				69.63	
	$I_f$				92.28	
	$I_{abs}$				161.91	
10.000	$I_{n,\gamma}$		41.44	64.20	69.78	70.57
	$I_f$		56.95	85.36	92.48	93.45
	$I_{abs}$		98.39	149.56	162.26	164.02
40.00	$I_{n,\gamma}$		48.53	66.46	69.81	70.58
	$I_f$		65.14	88.23	92.65	93.46
	$I_{abs}$		113.67	154.69	162.46	164.04

Resolved resonances: 1.14 ev ÷ 19.30 ev

TABLE 4B

## U-235 EFFECTIVE RESONANCE INTEGRALS FOR RESOLVED AND UNRESOLVED REGION

Temp.	Res.	Integr.	$\sigma_s^*$	10.75	40.75	110.75	$10^3$	$10^4$	$10^6$	$10^8$
300	$I_{n,\gamma}$			15.00	38.57	58.47	100.15	119.03	122.47	122.47
	$I_f$			28.44	69.78	102.77	165.71	192.35	197.18	197.18
	$I_{abs}$			43.44	108.35	161.24	265.86	311.38	319.65	319.65
2320	$I_{n,\gamma}$			17.61				117.87		
	$I_f$			33.62				189.01		
	$I_{abs}$			51.23				306.88		
5800	$I_{n,\gamma}$			18.51				115.39		
	$I_f$			35.35				183.72		
	$I_{abs}$			53.86				299.11		
10.000	$I_{n,\gamma}$			18.38		72.97		112.26	113.49	113.51
	$I_f$			34.66		119.92		177.36	179.23	179.26
	$I_{abs}$			53.04		192.89		289.62	292.72	292.77
40.000	$I_{n,\gamma}$							96.84		
	$I_f$							146.65		
	$I_{abs}$							243.49		

resolved resonances: 1.14 ev  $\div$  19.30 evunresolved resonances: 20 ev  $\div$  3 Kev (calculations inaccurate  
for  $T > 300^\circ K$ )

TABLE 5

ABSORPTION AND FISSION CROSS SECTIONS IN  
THE U-235 UNRESOLVED REGION

$E_{\min}$ (ev)	$E_{\max}$ (ev)	$\sigma_a$	$\sigma_f$
19.3	22.6	95.	60.
22.6	29.0	81.	46.
29.0	37.3	60.	40.
37.3	47.9	56.	36.
47.9	61.4	67.	47.
61.4	78.9	44.	24.
78.9	101.	44.	24.
101.	130.	29.5	21.
130.	167.	29.5	21.
167.	215.	28.5	20.
215.	275.	31.5	23.
275.	354.	22.5	14.
354.	454.	20.5	12.
454.	583.	23.5	15.
583.	748.	14.7	11.5
748.	961.	11.2	8.
961.	$1.23 \times 10^3$	12.6	9.4
$1.23 \times 10^3$	$1.59 \times 10^3$	10.0	6.8
$1.59 \times 10^3$	$2.04 \times 10^3$	9.4	6.2
$2.04 \times 10^3$	$2.61 \times 10^3$	9.4	6.2

TABLE 6A

CORRECTED EFFECTIVE RESONANCE INTEGRALS  
FOR U-235 (UNRESOLVED REGION)

T[°K]	Res. Integr.	$\sigma_s^*$		
		110.75	$10^4$	$10^8$
300	$I_{n,\gamma}$	29.14*	50.87*	58.58 (51.92*)
	$I_f$	58.23*	101.67*	106.89 (103.76*)
	$I_{abs}$	87.37*	152.74*	165.49 (155.68*)
10.000	$I_{n,\gamma}$		58.58	58.58
	$I_f$		106.91	106.91
	$I_{abs}$		165.49	165.49
40.000	$I_{n,\gamma}$		58.58	58.58
	$I_f$		106.91	106.91
	$I_{abs}$		165.49	165.49

\* Resonance integrals calculated by unrevised HRG-program.  
(in case of  $T = 300^\circ\text{K}$ ;  $\sigma_s^* = 10^8$ , listed for comparison)

TABLE 6B

CORRECTED EFFECTIVE RESONANCE INTEGRALS FOR  
U-235 (RESOLVED AND UNRESOLVED REGION)

T[°K]	Res. Integr.	$\sigma_s^*$		
		110.75	$10^4$	$10^8$
300	$I_{n,\gamma}$	58.47*	119.03*	129.13 (122.47*)
	$I_f$	102.77*	192.35*	200.33 (197.18*)
	$I_{abs}$	161.24*	311.38*	329.46 (319.65*)
10.000	$I_{n,\gamma}$		128.36	129.15
	$I_f$		199.39	200.36
	$I_{abs}$		327.75	329.51
40.000	$I_{n,\gamma}$		128.39	129.16
	$I_f$		199.56	200.37
	$I_{abs}$		327.95	329.53

\* Resonance integrals calculated by unrevised HRG-program.  
 (in case of  $T = 300^\circ\text{K}$ ;  $\sigma_s^* = 10^8$ , listed for comparison)

TABLE 7

## U-235 RESONANCE CROSS SECTIONS AT VARIOUS TEMPERATURES

(Calculated by HRG - and revised HRG program ( $B_1$  - approximation)  
with  $\sigma_s^* = 10^4$  and  $\sigma_s^* = 0.5 \times 10^4$ , and buckling  $B = 0.0225$ .)

IASL group # 8 9 10 11 12 13  
lower energy 0.55 kev 100. ev 30. 10. 3. 1.  
higher energy 3. kev 550. ev 100. 30. 10. 3.

$\hat{I} \hat{=} \sigma_s^* = 0.5 \times 10^4$ ;  $\hat{II} \hat{=} \sigma_s^* = 10^4$

$T = 300^\circ K$

group	$\sigma_{tr}$		$\sigma_a$		$\nu\sigma_f$		$\sigma_{n,\gamma}$		$\sigma_f$	
	I	II	I	II	I	II	I	II	I	II
8	17.54	17.55	6.99	7.00	11.32	11.35	2.33	2.33	4.66	4.67
9	27.01	27.08	16.70	16.78	27.05	27.17	5.57	5.59	11.13	11.18
10	57.64	58.35	47.79	48.51	77.39	78.57	15.94	16.18	31.85	32.33
11	111.54	115.27	102.65	106.51	142.80	148.04	43.88	45.59	58.77	60.92
12	65.00	66.57	54.71	56.29	78.19	80.45	22.53	23.19	32.18	33.11
13	41.36	41.49	31.23	31.34	52.02	52.21	9.82	9.86	21.41	21.48

TABLE 7 (cont'd.)

T = 2320°K													
group	$\sigma_{tr}$		$\sigma_a$		$\nu\sigma_f$		$\sigma_{n,\gamma}$		$\sigma_f$				
	I	II	I	II	I	II	I	II	I	II	I	II	
8	18.00	18.00	7.45	7.45	11.72	11.72	2.62	2.62	4.82	4.82			4.82
9	28.25	28.25	17.96	17.96	28.20	28.20	6.36	6.36	11.60	11.60			11.60
10	62.18	62.18	52.45	52.45	82.33	82.33	18.57	18.57	33.88	33.88			33.88
11	119.96	121.24	111.47	112.77	153.27	154.85	48.40	49.05	63.07	64.73			64.73
12	66.34	67.30	56.06	57.03	80.07	81.49	23.11	23.49	32.95	33.53			33.53
13	41.37	41.47	31.24	31.35	52.03	52.21	9.83	9.86	21.41	21.49			21.49

T = 5800°K													
group	$\sigma_{tr}$		$\sigma_a$		$\nu\sigma_f$		$\sigma_{n,\gamma}$		$\sigma_f$				
	I	II	I	II	I	II	I	II	I	II	I	II	
8	18.00	18.00	7.45	7.45	11.72	11.72	2.62	2.62	4.82	4.82			4.82
9	28.25	28.25	17.96	17.96	28.20	28.20	6.36	6.36	11.60	11.60			11.60
10	62.18	62.18	52.45	52.45	82.33	82.33	18.57	18.57	33.88	33.88			33.88
11	120.76	121.67	112.29	113.22	154.22	155.38	48.82	49.28	63.47	63.94			63.94
12	66.87	67.58	56.60	57.31	80.83	81.89	23.33	23.61	33.27	33.70			33.70
13	41.37	41.47	31.24	31.35	52.03	52.21	9.83	9.86	21.41	21.49			21.49



TABLE 7 (cont'd.)

T = 10,000°K												
group	$\sigma_{tr}$		$\sigma_a$		$\nu\sigma_f$		$\sigma_{n,\gamma}$		$\sigma_f$			
	I	II	I	II	I	II	I	II	I	II	I	II
8	18.00	18.00	7.45	7.45	11.72	11.72	2.62	2.62	4.82	4.82		
9	28.25	28.25	17.96	17.96	28.20	28.20	6.36	6.36	11.60	11.60		
10	62.18	62.18	52.45	52.45	82.33	82.33	18.57	18.57	33.88	33.88		
11	121.09	121.84	112.62	113.39	154.67	155.61	48.97	49.35	63.65	64.04		
12	67.12	67.71	56.85	57.45	81.22	82.09	23.43	23.67	33.42	33.78		
13	41.37	41.47	31.24	31.35	52.03	52.21	9.83	9.86	21.41	21.49		

T = 40,000°K												
group	$\sigma_{tr}$		$\sigma_a$		$\nu\sigma_f$		$\sigma_{n,\gamma}$		$\sigma_f$			
	I	II	I	II	I	II	I	II	I	II	I	II
8	18.00	18.00	7.45	7.45	11.72	11.72	2.62	2.62	4.82	4.82		
9	28.25	28.25	17.96	17.96	28.20	28.20	6.36	6.36	11.60	11.60		
10	62.18	62.18	52.45	52.45	82.33	82.33	18.57	18.57	33.88	33.88		
11	121.34	121.78	112.89	113.34	155.00	155.57	49.10	49.31	63.78	64.02		
12	67.54	67.90	57.28	57.64	81.87	82.42	23.58	23.72	33.69	33.92		
13	41.41	41.50	31.28	31.38	52.10	52.26	9.84	9.87	21.44	21.51		

TABLE 8A

## COMPARISON OF LASL-6 GROUP WITH HRG-6 GROUP CROSS SECTIONS

group	$E_L$	$E_M$	$\sigma_f$		$\sigma_{n,\gamma}$		$\sigma_{tr}$		$\nu$	
			LASL-6	HRG**	LASL-6	HRG	LASL-6	HRG	LASL	HRG
1	3	$\infty$ Mev	1.21	1.24	0.05	0.04	4.25	6.01	2.94	3.06
2	1.4	3.	1.22	1.29	0.08	0.06	4.50	6.2	2.62	2.67
3	0.9	1.4	1.22	1.25	0.11	0.11	4.65	5.59	2.53	2.57
4	0.4	1.9	1.20	1.24	0.15	0.17	5.20	6.1	2.49	2.50
5	0.1	0.4	1.43	1.52	0.23	0.33	7.9	8.89	2.46	2.46
	0.414 eV	0.1 Mev	25.2*	20.5	12.32*	10.4	47.35*	41.5	2.44	2.43

\* Weighted over  $1/E$  spectrum (see sec. 4.2)\*\*  $\sigma_s \approx 10^4$ ;  $T = 300^\circ K$ ;  $B = 0.0225$ .

TABLE 8B

COMPARISON OF LASL-16 GROUP WITH  
HRG-RESONANCE CROSS SECTIONS

LASL Group #	$\sigma_{n,\gamma}$		$\sigma_f$	
	LASL	HRG**	LASL	HRG**
8	3.2*	2.33	7.9*	4.67
9	8.5*	5.59	18.7*	11.18
10	20.	16.18	38.	32.33
11	32.7	45.59	51.7	60.92
12	39.2	23.19	42.8	33.11
13	8.8	9.86	30.	21.48

\* For infinite dilution.

\*\*  $\sigma_s \approx 10^4$ ;  $T = 300^\circ\text{K}$ ;  $B = 0.0225$ .

TABLE 9

INFLUENCE OF BUCKLING AND DILUTION ON THE HRG-RESONANCE CROSS SECTIONS

LASL group #	$\sigma_s^*$	buckling	LASL $\sigma_{n,\gamma}$	HRG	LASL $\sigma_f$	HRG
8	110.75	0.02245	3.2*	1.62	7.9*	3.25
		0.01		2.34		4.68
	10 <sup>4</sup>	0.02245		2.33		4.67
		0.045		2.32		4.64
		1/E-spectr.		2.35		4.70
9	110.75	0.02245	8.5*		18.7*	5.92
		0.01		5.60		11.19
	10 <sup>4</sup>	0.02245		5.59		11.18
		0.045		5.58		11.15
		1/E-spectr.		5.64		11.27
10	110.75	0.02245	18.8	7.79	35.85	15.57
		0.01		16.17		32.32
	10 <sup>4</sup>	0.02245	20.	16.18	38.	32.33
		0.045		16.20		32.37
		1/E-spectr.		16.26		32.50
11	110.75	0.02245	12.65	10.87	22.41	17.14
		0.01		45.60		60.92
	10 <sup>4</sup>	0.02245	32.7	45.59	51.7	60.92
		0.045		45.52		60.94
		1/E-spectr.		46.23		61.51
12	110.75	0.02245	22.77	10.21	23.43	15.38
		0.01		23.17		33.09
	10 <sup>4</sup>	0.02245	39.2	23.19	42.8	33.11
		0.045		23.22		33.17
		1/E-spectr.		23.15		33.04
13	110.75	0.02245	7.23	4.77	25.06	8.34
		0.01		9.87		21.51
	10 <sup>4</sup>	0.02245	8.8	9.86	30.	21.48
		0.045		9.82		21.37
		1/E-spectr.		9.95		21.78

\* For infinite dilution

TABLE 10

## RADIAL DEPENDENCE OF RESONANCE FLUXES

(Case A6:  $n_U = 1.129 \times 10^{19}$  at/cm<sup>3</sup>;  $n_H = 0$ .)

Radius [cm]	LASL - group number				
	8	9	10	11	12
0.6250	82538.	73209.	46141.	35960.	37644.
1.8750	82538.	73209.	46141.	35960.	37644.
3.1250	82538.	73209.	46141.	35961.	37644.
4.3750	82538.	73209.	46141.	35961.	37644.
5.6250	82538.	73209.	46141.	35961.	37645.
6.8750	82538.	73209.	46142.	35962.	37645.
8.1250	82538.	73209.	46142.	35962.	37645.
9.3750	82538.	73209.	46142.	35963.	37645.
10.6250	82538.	73209.	46142.	35963.	37645.
11.8750	82538.	73209.	46142.	35964.	37646.
13.1250	82538.	73209.	46143.	35965.	37646.
14.3750	82538.	73209.	46143.	35966.	37646.
15.6250	82538.	73209.	46143.	35967.	37646.
16.8750	82538.	73209.	46143.	35968.	37647.
18.1250	82538.	73210.	46144.	35969.	37647.
19.3750	82538.	73210.	46144.	35971.	37648.
20.6250	82538.	73210.	46145.	35972.	37648.
21.8750	82539.	73210.	46145.	35974.	37649.
23.1250	82539.	73210.	46146.	35975.	37649.
27.3750	82539.	73210.	46146.	35977.	37650.
25.6250	82539.	73210.	46147.	35979.	37650.
56.8750	82540.	73216.	46168.	36051.	37673.
58.1250	82540.	73216.	46169.	36055.	37675.
59.3750	82541.	73216.	46170.	36060.	37676.
60.6250	82541.	73217.	46172.	36064.	37677.
61.8750	82541.	73217.	46173.	36068.	37679.
63.1250	82541.	73217.	46174.	36072.	37680.
64.3750	82541.	73218.	46176.	36077.	37682.
65.6250	82541.	73218.	46177.	36082.	37683.
66.8750	82541.	73218.	46178.	36086.	37685.
68.1250	82541.	73219.	46180.	36091.	37686.
69.3750	82541.	73219.	46181.	36096.	37688.
40.6250	82541.	73219.	46183.	36101.	37689.
71.8750	82542.	73220.	46184.	36106.	37691.
73.1250	82542.	73220.	46186.	36111.	37692.
74.3750	82542.	73221.	46187.	36116.	37694.
75.6450	82542.	73221.	46189.	36121.	37696.
76.8750	82542.	73221.	46190.	36127.	37697.
78.1250	82542.	73222.	46192.	36132.	37699.
79.3750	82542.	73222.	46194.	36138.	37701.

TABLE 10A

## RADIAL DEPENDENCE OF THERMAL FLUXES

(Case C5; interior compression;  $P_{int} = 1/2$ .)

Radius [cm]	LASL - groups			
	1-3 ev G = 13	0.4-1 ev 14	0.1-0.4 ev 15	therm. 16
0.5000	22102.	9996.	1161.	6.
1.5000	22105.	10004.	1167.	7.
2.5000	22111.	10019.	1180.	7.
3.5000	22120.	10042.	1200.	8.
4.5000	22132.	10073.	1227.	9.
5.5000	22148.	10112.	1261.	11.
6.5000	22166.	10159.	1302.	13.
7.5000	22188.	10213.	1351.	16.
8.5000	22212.	10276.	1409.	21.
9.5000	22240.	10346.	1476.	26.
10.5000	22271.	10425.	1553.	33.
11.5000	22305.	10512.	1640.	43.
12.5000	22342.	10608.	1738.	56.
13.5000	22382.	10712.	1849.	73.
14.5000	22426.	10825.	1974.	97.
15.5000	22472.	10947.	2114.	128.
16.5000	22522.	11077.	2270.	170.
17.5000	22575.	11217.	2444.	227.
18.5000	22631.	11367.	2639.	304.
19.5000	22691.	11526.	2855.	409.
20.5000	22753.	11695.	3097.	550.
21.5000	22819.	11873.	3365.	742.
22.5000	22888.	12063.	3664.	1004.
23.5000	22960.	12263.	3996.	1361.
24.5000	23036.	12473.	4366.	1847.
25.5000	23115.	12695.	4778.	2512.
26.5000	23197.	12929.	5236.	3422.
27.5000	23282.	13174.	5745.	4668.
28.5000	23371.	13432.	6313.	6375.
29.5000	23464.	13702.	6944.	8718.
30.5000	23560.	13985.	7647.	11936.
31.5000	23659.	14281.	8431.	16359.
32.5000	23761.	14592.	9303.	22443.
33.5000	23868.	14916.	10276.	30820.
34.5000	23977.	15255.	11361.	42362.
35.5000	24090.	15609.	12570.	58275.
36.5000	24207.	15979.	13919.	80230.
37.5000	24328.	16366.	15425.	110538.
38.5000	24452.	16769.	17105.	152405.
39.5000	24579.	17189.	18981.	210272.

TABLE 11

DATA FOR SPHERICAL EXPERIMENTAL REACTORS

Sphere 1

Zone	Be-island	fuel	Be-refl.	C-refl.
Radii [cm]	15.2	22.3	51.6	70.3
Mesh width in zone for computations*	5.07	2.367	9.8	9.35
Atomic dens. [at/cm <sup>3</sup> ]	$1.434 \times 10^{23} **$	***	$1.135 \times 10^{23} **$	$7.35 \times 10^{22} **$

\* Not checked for space differencing errors.

\*\* Together with  $3.0 \times 10^{21}$  Al-atoms/cm<sup>3</sup> accounting for the presence of structural materials.

\*\*\* The fuel was 10 unit Oy-foils (93.4 per cent U-235) separated by canned sodium. Sodium content in fuel region was approximately  $2.51 \times 10^{22}$  at/cm<sup>3</sup>.

Sphere 2

Zone	Be-island	fuel	Be-refl.	C-refl.
Radii [cm]	11.43	22.8	52.6	68.6
Mesh width in zone for computations*	2.29	0.568	2.29	2.
Atomic dens. [at/cm <sup>3</sup> ]	$1.434 \times 10^{23} **$	***	$1.135 \times 10^{23} **$	$7.74 \times 10^{22} **$

\* Checked for space differencing errors.

\*\* Together with  $3.0 \times 10^{21}$  Al-atoms/cm<sup>3</sup> accounting for presence of structure materials.

\*\*\* Together with mixture of  $1.68 \times 10^{21}$  C-at/cm<sup>3</sup>,  $1.0 \times 10^{21}$  Zr-at/cm<sup>3</sup>, and  $2.39 \times 10^{22}$  Na-at/cm<sup>3</sup> to simulate a fused fluoride.

TABLE 11 (cont'd.)

Sphere 3

Zone	Be-island	fuel	SS-316*	Be-refl.	C-refl.
Radii [cm]	11.43	22.8	23.1	52.6	68.6
Mesh width in zone for computations **	2.29	0.568	0.3	2.27	2.
Atomic dens. [at/cm <sup>3</sup> ]	$1.434 \times 10^{22}$	****	$8.47 \times 10^{22}$	$1.135 \times 10^{23}$	$7.74 \times 10^{22}$

\* Sphere 3 had an additional 0.3 cm of SS-316 simulating shells to contain the fluoride.

\*\* Checked for space differencing errors.

\*\*\* Together with  $3.6 \times 10^{21}$  Al-atoms/cm<sup>3</sup> accounting for the presence of structural materials.

\*\*\*\* Together with the simulated fused fluoride mixture (see sphere 2).



TABLE 12

DATA FOR CYLINDRICAL EXPERIMENTAL REACTORS

Dimensions\* (see Fig. 10):  $h_{\text{tot}} = 85.1 \text{ cm}$   
 $h_c = 39.37 \text{ cm}$   
 $r_c = 19.685 \text{ cm}$   
 $t_1 = 46.99 \text{ cm}$   
 $t_2 = 45.73 \text{ cm}^{**}$

\* The high number of significant figures is a result of the conversion from inches to cm.

\*\* In the actual experiment the bottom reflector was 3" shorter than the top reflector. In the recalculation both top and bottom reflectors are assumed to have a thickness of 18". This is partly compensated by the Al-base-plate used in the experiments.

Material data: Be-atomic density =  $1.195 \times 10^{23} \text{ atoms/cm}^3$ ;  
Oy with 93.15 per cent U-235 and 6.85 per cent U-238; fuel elements with 22.02 per cent Oy and 77.98 per cent graphite.

## REFERENCES

1. Holl, R.J., "Cavity Nuclear Reactors," Douglas Paper No. 1738, July, 1963.
2. Hyland, R.E. et al, "Two Dimensional Criticality Calculations of Gaseous-Core Cylindrical-Cavity Reactors," NASA TN D-1575, March, 1963.
3. Joanou, G.D., and Dudek, J.S., "GAMI: A Consistent P Multigroup Code for the Calculation of Fast Neutron<sup>1</sup> Spectra and Multigroup Constants," GA-1850, June, 1961.
4. Dresner, L., Resonance Absorption in Nuclear Reactors, Pergamon Press, 1960.
5. Adler, F.T. et al, "The Quantitative Evaluation of Resonance Integrals," United Nations Conference on the Peaceful Uses of Atomic Energy, 1958, Vol. 16, p. 155.
6. Schermer, R., Corngold, N., "Resonance Capture of Neutrons in Infinite Homogeneous Media," Proc. Phys. Soc., Vol. LXXIII, p. 561, 1959.
7. Weinberg, A.M., Wigner, E.P., The Physical Theory of Neutron Chain Reactors, The University of Chicago Press, 1958.
8. Macklin, R.L., Pomerance, H.S., "Resonance Capture Integrals," United Nations Conference on the Peaceful Uses of Atomic Energy, 1958, Vol. V, p. 96.
9. Hughes, D.J., Schwartz, R.B., "Neutron Cross Sections," BNL 325 (2nd Ed.).
10. Hansen, G.E., Roach, W.H., "Six and Sixteen Group Cross Sections for Fast and Intermediate Critical Assemblies," LAMS-2543, Nov., 1961.
11. Hassitt, A., "CRAM, A Computer Program to Solve the Multigroup Diffusion Equations," TRG Report 229 (R), United Kingdom Atomic Energy Authority, Risley, Warrington, Lancashire, 1962.

12. Mills, C.B., "Reflector Moderated Reactors," Nucl. Sci. and Eng: 13, 301-305, 1962.
13. Safonov, G., "Externally Moderated Reactors," Second United Nations International Conference on the Peaceful Uses of Atomic Energy, P/625, June, 1958.
14. Jarvis, G.A. and Byers, C.C., "Beryllium - Reflected Cavity Reactor Experiment," N-2-7094 (Deleted), Nuclear Propulsion Division Progress Report for Sept. 11, 1962, Los Alamos Scientific Laboratory.
15. Carlson, B.G., "Solution of the Transport Equations by  $S_n$  Approximations," LA-1891, Los Alamos Scientific Laboratories, 1955.
16. Ragsdale, R.G. and Hyland, R.E., "Some Nuclear Calculations of U-235 - D O Gaseous - Core Cavity Reactors," NASA TND-475, Oct<sup>2</sup>, 1961.
17. Gotsky, E.R., Cusick, J.M., and Bogart, D., "Two-Dimensional Diffusion Theory Analysis of Reactivity Effects of a Fuel-Plate-Removal Experiment," NASA TR R-36, 1959.
18. Butler, W.R. and Chang, H.C., "A Transport Theory Analysis of a Gaseous Core Concept," RN-TM-0190, May 1965.

### ACKNOWLEDGEMENTS

I should like to thank Professor R. A. Gross and Professor R. W. Houston for suggesting this problem and for their continuous interest and invaluable guidance without which this work could not have been completed.

I also find it a great pleasure to thank Mr. J. L. Carter, Dr. G. A. Jarvis, and Dr. R. G. Ragsdale for valuable and interesting suggestions.

I am indebted to the National Aeronautics and Space Administration, the European Space Research Organization, and the German Ministry for Scientific Research who jointly granted my present International University Fellowship in Space Science. This report has been supported by the Air Force Office of Scientific Research under Contract AF 49(638)1254.